“ALEXANDRU IOAN CUZA" UNIVERSITY OF IAȘI

FACULTY OF CHEMISTRY

DOCTORAL SCHOOL OF CHEMISTRY

Oxide nanomaterials for photocatalytic applications

PhD THESIS SUMMARY

PhD supervisor,

Prof. univ. dr. **Aurel PUI**

PhD student,

Chem. **Ioana RADU**

IASI

2025

DOCTORAL COMMITTEE:

President:

Prof. univ. dr. habil. **Cecilia ARSENE**

"Alexandru Ioan Cuza" University of Iași

PhD supervisor:

Prof. univ. dr. **Aurel PUI**

"Alexandru Ioan Cuza" University of Iași

Scientific referees:

Prof. univ. dr. **Adelina Carmen IANCULESCU**

POLITEHNICA University of Bucharest

Prof. univ. dr. habil. **Gabriela-Nicoleta NEMEȘ**

"Babes Bolyai" University of Cluj Napoca

Prof. univ. dr. **Alexandra Raluca IORDAN**

"Alexandru Ioan Cuza" University of Iași

The results presented in the doctoral thesis represent the synergic result between the own work and the fruitful collaborations realized during the doctoral stage.

The concept, synthesis of the materials, photocatalytic tests and part of the analysis were carried out at the Faculty of Chemistry of the "Alexandru Ioan Cuza" University of Iasi, while the other analysis and measurements were carried out in collaboration with different academic/research institutions:

Faculty of Physics of "Alexandru Ioan Cuza" University of Iasi: *X-ray diffraction analysis, magnetic and electrical measurements*

National Research and Development Institute for Materials Physics (Magurele): *XPS analysis*

National Research-Development Institute for Technical Physics from Iasi: *SEM/TEM analysis*

Paul Scherrer Institute (Switzerland): *XAS synchrotron analysis*

Elettra-Sincrotron Institute Trieste (Italy): *synchrotron XPS analysis*

Table of contents

PART I – LITERATURE REVIEW

INTRODUCTION

Nanomaterials, the key building blocks of nanotechnology, are materials with particle sizes smaller than 100 nm that exhibit physico-chemical properties significantly different from those of macromolecular structures with the same composition. Oxide nanomaterials play an important role in many fields and subfields, such as chemistry, physics, biology, materials science, and constitute one of the most common, diverse and probably the richest class of materials. Unlike other classes of materials, nanostructured metal oxides are characterized by a wide and fascinating range of properties and are widely used, in particular due to their high thermal and chemical stability [5–8]. Spinel ferrites are a category of oxide nanomaterials intensively studied due to their magnetic, electrical, optical and catalytic properties. Another category of nanostructured metal oxide nanostructures are perovskite-type oxides. They exhibit attractive physico-chemical properties, which allow these materials to be used in optoelectronic applications, photovoltaics, photocatalysis or as electrochemical sensors.

Starting from the role and importance of nanomaterials, especially oxide nanomaterials, in the present PhD thesis we aimed to synthesize oxide nanomaterials exhibiting enhanced photocatalytic activity. Aluminum-doped perovskite-type oxides ($Al_{x\%}$:$SrTiO_3$) constitute another class of nanostructured oxide nanostructures studied. To improve the photocatalytic activity of perovskite-type materials they were functionalized with oxyhydroxide structures.

PART II – PERSONAL CONTRIBUTIONS

MOTIVATION FOR THE RESEARCH TOPICS

Globally, energy and environmental issues are important topics, therefore development of new systems to solve the problems caused by the intensive use of fossil fuels and the inefficiency of traditional methods used to remove organic contaminants from wastewater is essential. Considering the sustainability of solar energy, special attention was awarded to the use of photocatalytic oxidation to remediate environmental problems, photocatalysis representing a major breakthrough for sustainable, non-toxic and economically viable technologies. The major challenge in photocatalysis today remains the development of photocatalytic systems with extended photocatalytic activity to the visible region of the solar spectrum. An efficient photocatalyst must have high specific surface area, superior sensitivity to the visible region of the solar spectrum, suitable electronic band positions and efficient charge carrier transport to inhibit recombination. The doping of perovskite-structured oxides by introducing aliovalent cations into their structure has been shown to be an effective strategy for modifying functional properties such as optical absorption, p/n characteristics, charge density, charge mobility and separation, particle size, crystallinity, hydrophilicity and defect density.

Based on these considerations, the aim of the PhD thesis was the synthesis and characterization of oxide nanomaterials for photocatalytic applications.

The studies carried out during the doctoral studies were focused on the design of novel, high-efficiency photocatalytic materials that exploit a wide part of sunlight and which are able to address two of the major challenges for sustainable development, namely the removal of organic contaminants from wastewater and the production of H_2 through photocatalytic water splitting.

In order to achieve the aim of the thesis the following main objectives were proposed:

O_1. Synthesis, characterization and evaluation of the potential use of Zn-Mn mixed ferrite nanoparticles substituted with Gd^{3+} ions as photocatalysts in the photodegradation of rhodamine B under visible radiation.

O_2. Synthesis, characterization and investigation of the electronic properties of $SrTiO_3$ doped with Al^{3+} ions.

O_3. Evaluation of the photocatalytic efficiency of $Al_{x\%}$:$SrTiO_3$ materials in the degradation process of Orange IV dye, as well as in the photocatalytic water splitting.

O_4. Development of $Al_{3\%}$:$SrTiO_3$@MOOH (M = Fe, Co) photocatalytic nanoreactors by surface functionalization of perovskite particles, $Al_{3\%}$:$SrTiO_3$ with metal oxyhydroxides and their characterization.

O_5. Evaluation of the photocatalytic efficiency of $Al_{3\%}$:$SrTiO_3$@δ-FeOOH and $Al_{3\%}$:$SrTiO_3$@CoOOH nanoreactors in photocatalytic degradation processes of different pollutants (Orange IV, Tetracycline, Oxacillin) under visible light.

III. SPINEL-TYPE OXIDE NANOMATERIALS SUBSTITUTED WITH RARE METAL IONS

III.1. Synthesis of $Zn_{0,7}Mn_{0,3}Fe_2O_4$ nanoparticles substituted with Gd^{3+} ions

Ferrite nanoparticles $Zn_{0,7}Mn_{0,3}Gd_xFe_{2-x}O_4$ (x = 0; 0.025; 0.05; 0.075; 0.1) were synthesized by a wet-chemical method developed within the research group [88]. The method used involves co-precipitation of oxide nanoparticles from precursor solutions in a basic medium**,** in the presence of a surfactant. In order to stabilize the structure and obtain a high crystallinity degree of the synthesized nanoparticles, they were thermally treated at 500 ºC for six hours.

III.2. Characterization of $Zn_{0,7}Mn_{0,3}Fe_2O_4$ nanoparticles substituted with Gd^{3+} ions

The X-ray diffractograms recorded for $Zn_{0.7}Mn_{0.3}Gd_xFe_{2-x}O_4$ nanoparticles treated at 500 °C which are illustrated in figure III.2a indicate the presence of a single crystallographic phase attributed to the cubic spinel structure, characterized by the Fd-3m space group.

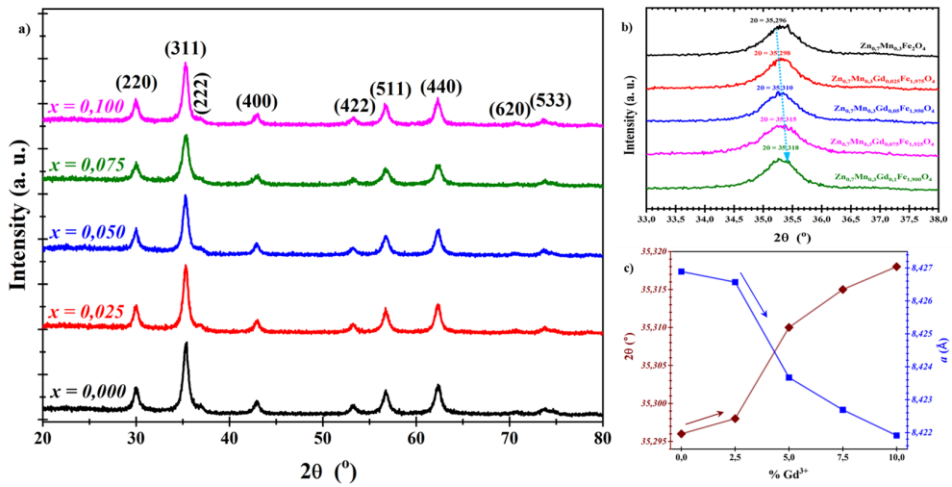

Figure III.2. *(a) X-ray diffractograms of Gd^{3+}-substituted ferrite samples treated at 500 °C; (b) the change in the position of the (311) reflection with increasing Gd^{3+} content and (c) the variation of the lattice constant and the position of the corresponding (311) plane reflection with respect to the Gd^{3+} content.*

III.2.3. Morphology analysis by SEM microscopy

The morphology of Zn-Mn ferrite samples treated at 500 ℃ was analyzed by SEM microscopy and the obtained images are shown in figure III.4a-e. The nanometric size of the ferrite particles is confirmed by FE-SEM images, these indicating the formation of spherical, agglomerated particles with an average size in the range of 20-30 nm.

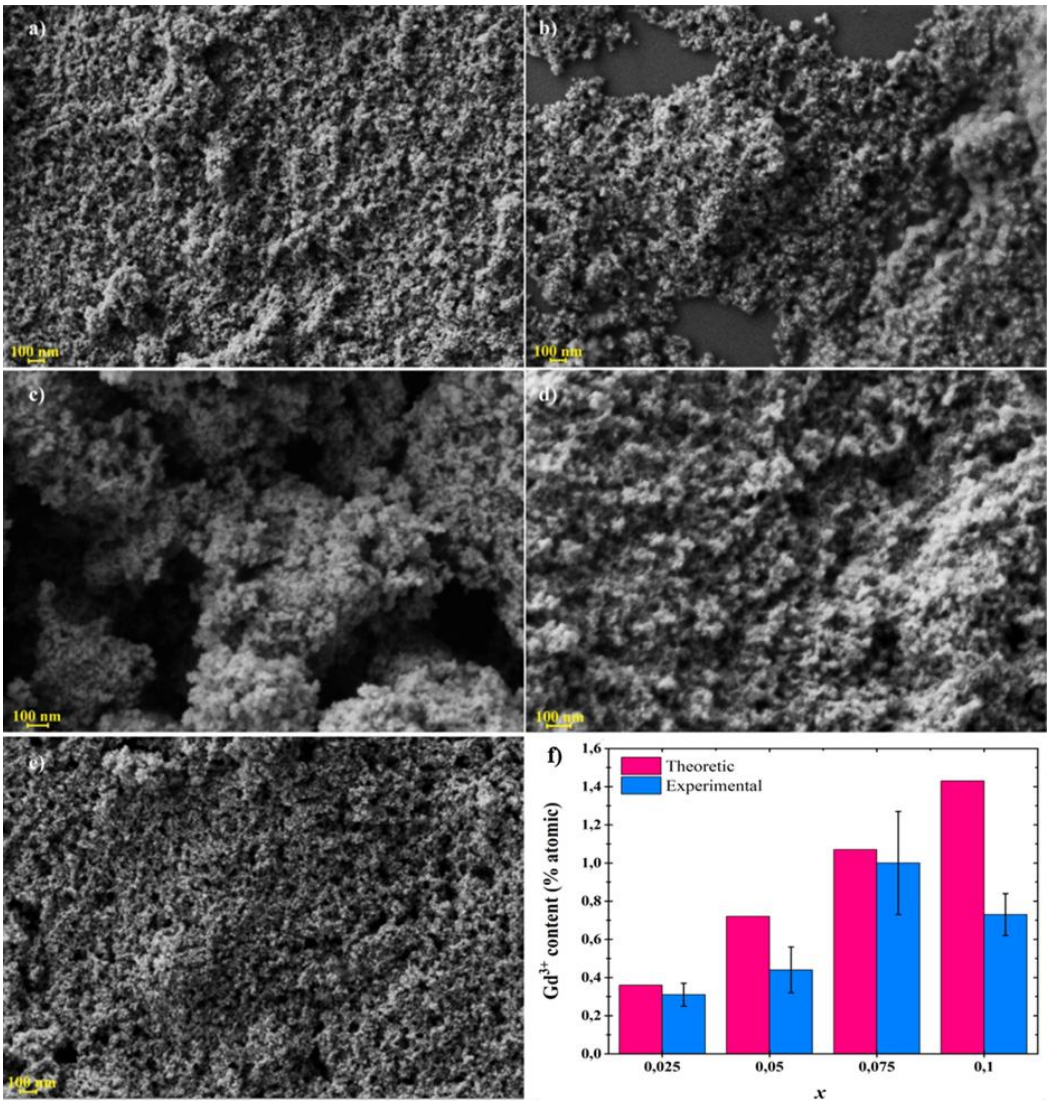

Figure III.4. *FE-SEM images of $Zn_{0,7}Mn_{0,3}Gd_xFe_{2-x}O_4$ nanoparticles in which: (a) x = 0.000; (b) x = 0.025; (c) x = 0.050; (d) x = 0.075; (e) x = 0.100; and (f) variation of experimental Gd^{3+} content with respect to theoretical composition.*

III.3. Photocatalytic efficiency evaluation of $Zn_{0,7}Mn_{0,3}Gd_xFe_{2-x}O_4$ oxide nanomaterials in Rhodamine B photodegradation

To evaluate the photocatalytic performance of the synthesized Gd^{3+} ion-substituted ferrite samples, a series of photocatalytic degradation tests of rhodamine B under visible light radiation were performed. Figure III.9 shows, for all the samples analyzed, a decrease in the absorbance of the maximum located at 555 nm, which indicates that the synthesized materials exhibit photocatalytic activity under visible light radiation. As for the photocatalytic process, it can be observed that it shows specific particularities depending on the composition and the thermal treatment applied to the materials. Thus, for unsubstituted ferrite (x = 0.000), treated at 500 °C, a decrease in the absorption maximum is observed, which after the first 75 minutes is accompanied by a hypochromic shift of its absorption maximum and the formation of a new absorption maximum around ≈ 500 nm, the efficiency of the photocatalytic process being about 80% after 180 minutes of irradiation. For the sample with the same composition, treated at 650 °C, the absorption spectra show a similar behavior, being characterized by the same shift towards the formation of a new absorption maximum, with the difference that, in this case, the efficiency of the photocatalytic reaction is higher, being ≈ 93% after 180 minutes of irradiation.

Thus, the obtained experimental results and the available information in the literature suggest that the formation of the new absorption maximum around 500 nm and the change in the emission maximum of the rhodamine B solution at the end of the photocatalytic process are associated with the formation of the Rh110 derivate, which results from the rhodamine deethylation process. According to the mechanism presented by Jakimińska *et al.*, the deethylation process occurs when the photocatalyst is activated by excited Rhodamine (RhB*) molecules with visible light, while direct excitation of the photocatalyst results in the decomposition of the chromophore in the RhB structure.

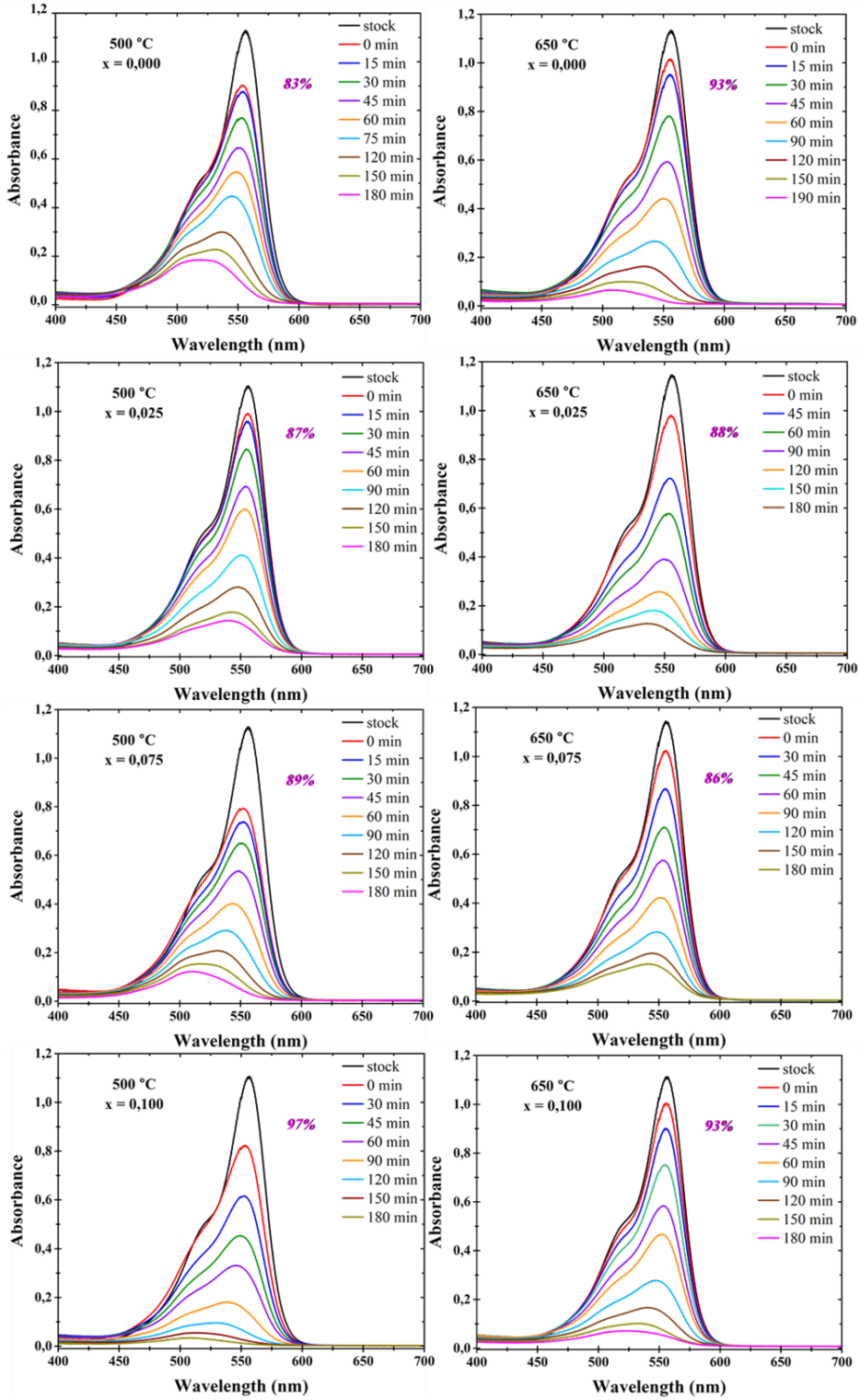

Figure III.9. *UV-Vis absorption spectra of Rhodamine B, recorded during the photocatalytic experiments in which ferrite samples, $Zn_{0,7}M_{0,3}Gd_xFe_{2-x}O_4$, were used as photocatalysts.*

III.4. Assessment of the potentials of $Zn_{0,7}Mn_{0,3}Gd_xFe_{2-x}O_4$ as acetone sensors

From figure III.11 it can be seen that, for all samples, the real part of the impedance decreases in the presence of acetone vapor during each cycle, with a tendency towards saturation. In the immersion time of ~200 s (arbitrarily chosen), the value of R decreases to 67% (x = 0.000), 58% (x = 0.025), 62% (x = 0.050), 55% (x = 0.075) and 53% (x = 0.100) of the initial value (R_{air}), without reaching a saturation level. Figure III.11g shows that the response time of the $Zn_{0.7}Mn_{0.3}Fe_{2-x}Gd_xO_4$ ferrite samples to the presence of acetone vapor varies in the range 36-56 s, it closely follows the trend of the porosity grade. The recovery time of the $Zn_{0.7}Mn_{0.3}Fe_{2-x}Gd_xO_4$ samples varies between 80 and 116 s (fig. III.11h), and its trend is closely related to the R/R_{air} value reached by samples after the 200 s exposure in air saturated with acetone vapors.

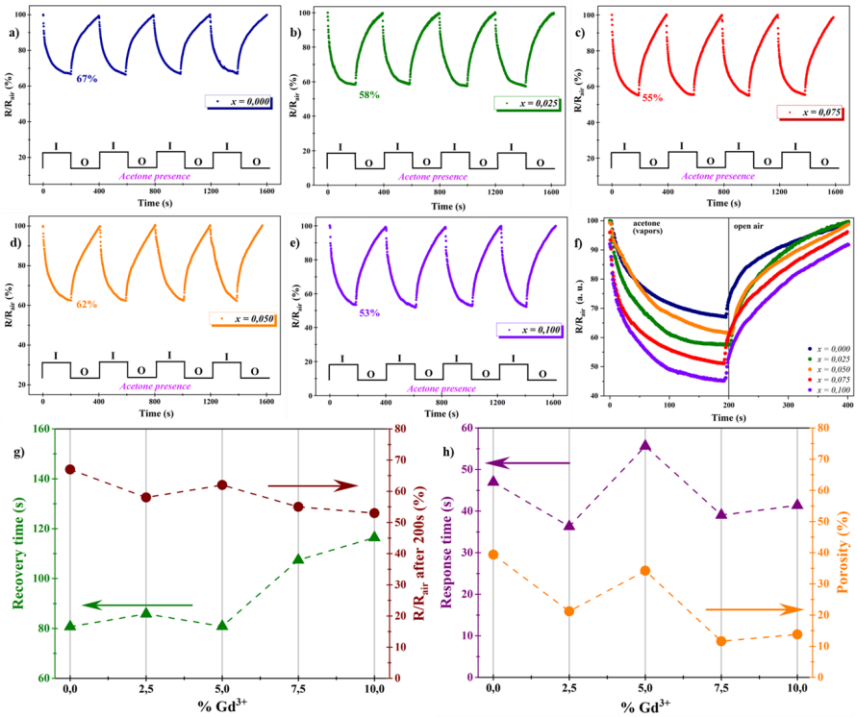

Figure III.11. *(a-e) Sensitivity of $Zn_{0.7}Mn_{0.3}Fe_{2-x}Gd_xO_4$ samples after exposure for four cycles to air saturated with acetone vapor at room temperature; (f) sensitivity of all samples during a single exposure cycle; (g) variation of response time to acetone vapor in relation to sample porosity and Gd^{3+} content; (h) variation of recovery time in free air in relation to Gd^{3+} and R/R_{air} content.*

IV. STRONTIUM TITANATE DOPED WITH Al3+ IONS

IV.1. Synthesis and characterization of $SrTiO_3$ doped with Al^{3+} ions

Al^{3+} doped $SrTiO_3$ ($Al_{x\%}$:$SrTiO_3$) materials were synthesized using the ceramic method and the dopant content used was in the range 0-10% (mass %). For simplicity, the obtained materials will be named using the notation $Al_{x\%}$:$SrTiO_3$, corresponding to each percentage of Al^{3+}.

IV.1.2. Structural analysis by X-ray diffraction

The X-ray diffractograms recorded for the $Al_{x\%}$:$SrTiO_3$ samples (fig. IV.1a) show specific reflections corresponding to the perovskite structure, without supplementary reflections specific to the Al_2O_3 compound used as a precursor for doping. These indicate that the method used led to the formation of a single crystalline phase, the perovskite phase characteristic of strontium titanate.

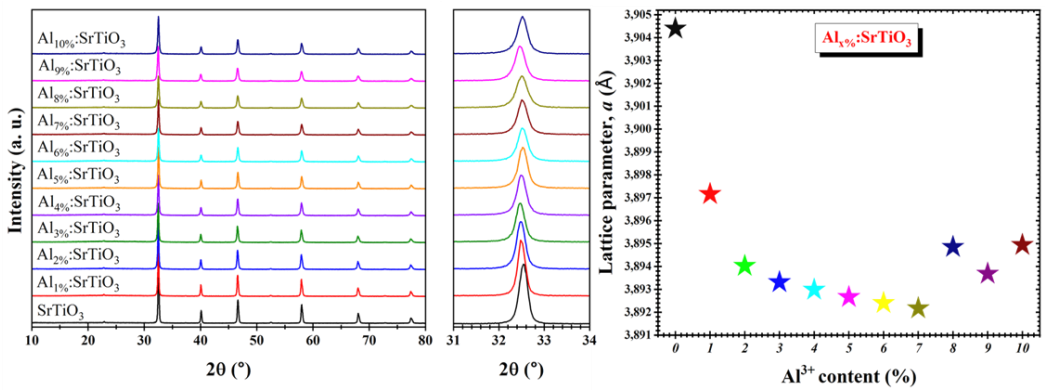

Figure IV.1. *a) X-ray diffractograms recorded for pure and Al^{3+} doped $SrTiO_3$ samples, highlighting the shift of the main reflection for the doped samples; b) variation of the lattice parameter as a function of the doping considered.*

From the structural point of view, all the obtained samples belong to the Pm-3m symmetry group specific to the cubic perovskite $SrTiO_3$. The introduction of aluminum (Al^{3+}) determines a shift in the position of the main reflection on the 2θ axis from 32.35° to 32.52°, which is reflected in the lattice parameter, characterized by a relatively uniform variation only for samples with Al^{3+} content in the range 3-7% (fig. IV.1b).

IV.1.4. Morphology analysis by SEM microscopy

Figure IV.4 shows the FE-SEM images recorded for $Al_{x\%}$:$SrTiO_3$ materials at different magnifications. From the FE-SEM images it can be observed that both the pure $SrTiO_3$ and the Al^{3+} doped $SrTiO_3$ samples ($Al_{x\%}$:$SrTiO_3$) are characterized by particles with cubic morphology, for the doped samples, the cubic morphology is slightly deformed and the particles are not very clearly defined. Also, a reduction of particle size is observed with the increasing of Al^{3+} content.

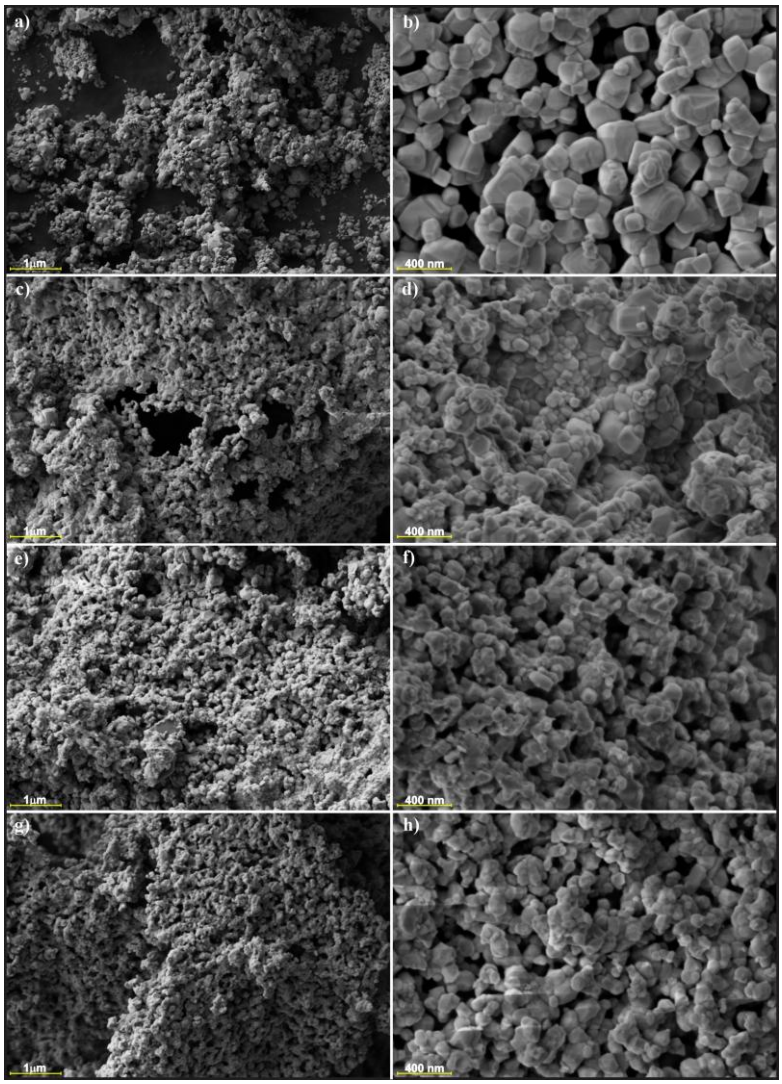

Figure IV.4. *FE-SEM images at different magnifications for $SrTiO_3$ (a-b), $Al_{3\%}$:$SrTiO_3$ (c-d), $Al_{7\%}$:$SrTiO_3$ (e-f) and $Al_{10\%}$:$SrTiO_3$ (g-h), respectively.*

IV.1.5. Electronic structure investigation by XPS

The XPS spectra of Ti *2p* for Al-doped $SrTiO_3$ samples, and their decomposition into components characteristic of the different oxidation states of titanium ($Ti^{4+}/Ti^{3+}/Ti^{2+}$) are shown in figure IV.5. The analysis of the Ti *2p* characteristics indicates a mixed contribution from the ideal octahedral geometry of titanium (Ti^{4+}), accompanied by Ti^{3+} and Ti^{2+} states, respectively, which are most frequently associated with the presence of oxygen vacancies (V_OS). It is noteworthy that, Ti^{2+} species are found only in the sample corresponding to the highest percentage of Al^{3+} doping, $Al_{10\%}$:$SrTiO_3$.

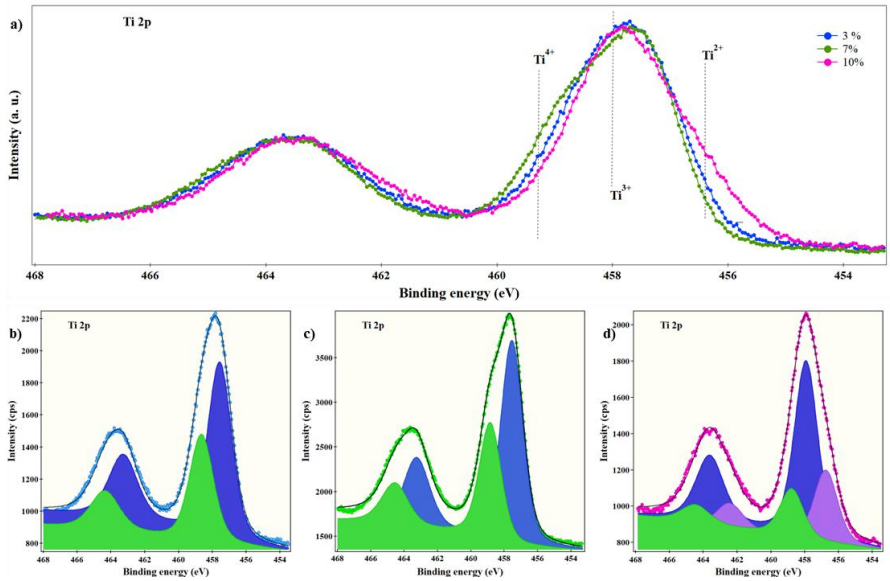

Figure IV.5. *XPS spectra of Ti 2p recorded for $Al_{3\%}$:$SrTiO_3$, $Al_{7\%}$:$SrTiO_3$ and $Al_{10\%}$:$SrTiO_3$ samples (a); individual and simulated XPS spectra for $Al_{3\%}$:$SrTiO_3$ (b), $Al_{7\%}$:$SrTiO_3$ (c) and $Al_{10\%}$:$SrTiO_3$ (d).*

The ratio between the integral amplitudes of the corresponding Ti^{4+} and Ti^{3+} components, obtained as individual spectra (Fig. IV.5(b-d)), shows that Ti^{3+} species are predominant in all samples. This can be explained by assuming an itinerant character of the oxygen vacancies, which will diffuse through the $SrTiO_3$ lattice and accumulate more at its surface, where they are detected by XPS measurements [123–126].

Also, in the case of the $Al_{10\%}$:$SrTiO_3$ sample, the asymmetry of the Ti *2p* XPS spectrum and its shift towards lower binding energies is a clear signature of a lower state, Ti^{2+}, which can occur by the formation of two mono-ionized oxygen vacancies ($V_O^{\bullet}$) or a single double-ionized oxygen vacancy ($V_O^{\bullet\bullet}$) [127]. Such variation is a clear indication that with increasing Al doping more V_Os are created to maintain the neutrality of the system.

The simulated individual spectra of O *1s* are presented in figure IV.6c-e for $Al_{3\%}$:$SrTiO_3$, $Al_{7\%}$:$SrTiO_3$ and $Al_{10\%}$:$SrTiO_3$, while the individual spectra for Sr 3d are shown in Figure IV.6(f-h). Thus, the increase in Al^{3+} doping results in the appearance of asymmetry of the XPS spectrum of Sr *3d* in the region of lower binding energies, accompanied by a decrease in the signal intensity for O *1s* corresponding to oxygen atoms in the surround determined by the perovskite lattice.

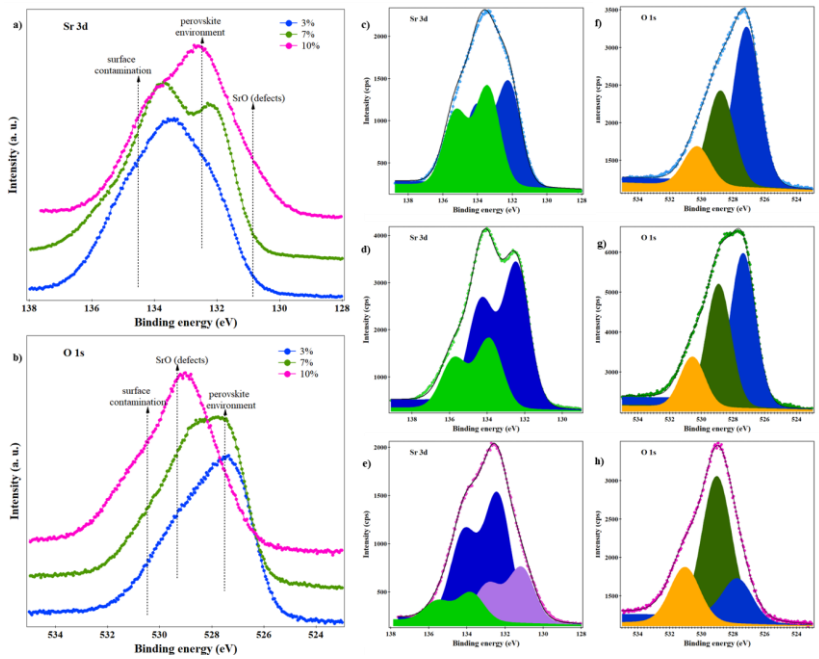

Figure IV.6. *XPS spectra of Sr 3d (a) and O 1s (b) recorded for $Al_{3\%}$:$SrTiO_3$, $Al_{7\%}$:$SrTiO_3$ and $Al_{10\%}$:$SrTiO_3$. The simulation of the individual spectra with Voigt lines representing different components for the $Al_{3\%}$:$SrTiO_3$, $Al_{7\%}$:$SrTiO_3$and $Al_{10\%}$:$SrTiO_3$ samples is shown in figures (c-e) for O 1s, and (f-h) for Sr 3d, respectively.*

The main component which appears at 132.5 eV corresponds to Sr^{2+} cations in $SrTiO_3$, while the component at higher binding energies is associated with $SrCO_3$ and $Sr(OH)_2$ species from surface contamination. For the sample corresponding to the highest doping level, $Al_{10\%}$:$SrTiO_3$, the appearance of a component at lower binding energies corresponding to strontium oxide, SrO, is observed. This state results from the substitution of the Sr^{2+} cations by Al^{3+} cations, when the substituted strontium diffuses through $SrTiO_3$ and reacts, reaching at the surface as SrO, where it acts as a defect.

Doping with Al causes a concomitant shift to higher energies of the entire characteristic spectra O *1s* and Sr *3d*, respectively, which is also slightly observed, in the corresponding XPS spectrum Ti *2p* (fig. IV.5). This shift can be explained by the oxidized Al/$SrTiO_3$ interface, which gradually evolves with increasing Al^{3+} content. Consequently, the conduction states in $SrTiO_3$ gradually fills, defining in the contact region a metallic conduction zone in the form of a two-dimensional electron gas (2DEG).

IV.1.6. Electronic structure investigation by XAS

Figure IV.7 shows the spectra recorded at the aluminum K-level in total fluorescence yield (TFY) detection mode for the samples $Al_{3\%}$:$SrTiO_3$, $Al_{7\%}$:$SrTiO_3$ and $Al_{10\%}$:$SrTiO_3$. The shape of the spectra of the three samples is similar, with a broad contribution before the main absorption band located at 1569 eV. The broad feature indicates the presence of disordered Al sites with less than 6 nearest O neighbors. According to the literature [129] and the reference spectra for Al_2O_3 presented in figure IV.7, the signature of the tetrahedral coordination is located at 1566 eV, while the octahedral atomic coordination generates features at 1567 eV and 1569 eV. Thus, we can conclude that, Al is mainly characterized by an octahedral symmetry in bulk, with a significant amorphous deformation being observed in the spectrum of the sample corresponding to the 7% Al doping, compared to the sample containing 10% Al.

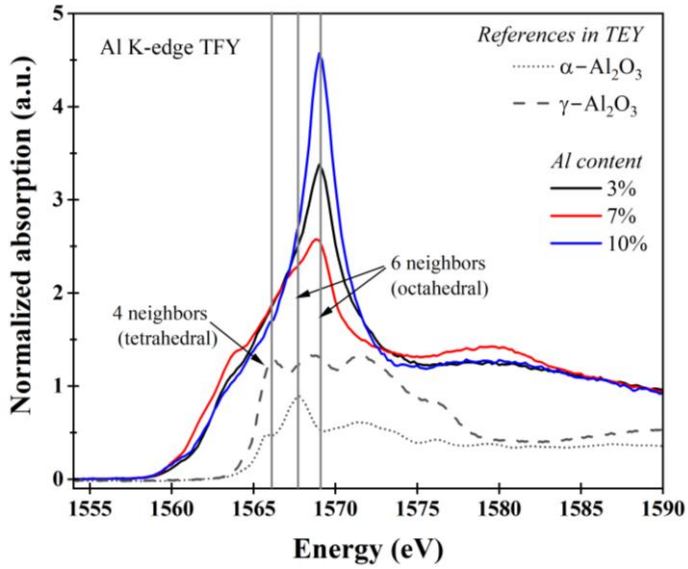

Figure IV.7. *XAS spectra recorded at the K level of aluminum for $Al_{3\%}:SrTiO_3$, $Al_{7\%}:SrTiO_3$ and $Al_{10\%}:SrTiO_3$ Samples.*

Figure IV.8a shows the typical Ti^{4+} $L_{2,3}$-edges split by the crystal field into e_g and t_{2g} components, dominated by dipole transitions between Ti *2p* and Ti *3d* energy levels. The width of the maximum corresponding to the e_g component located at 459.9 eV was analyzed for each of the three doping levels, the results being shown in fig. IV.8a, where an increase in the width of the maximum is observed with the increasing of Al^{3+} doping level. This increase in the width of the maximum characteristic of the e_g component, as well as the asymmetry of the maximum, can be explained by the presence of Ti^{3+} and Ti^{2+} states.

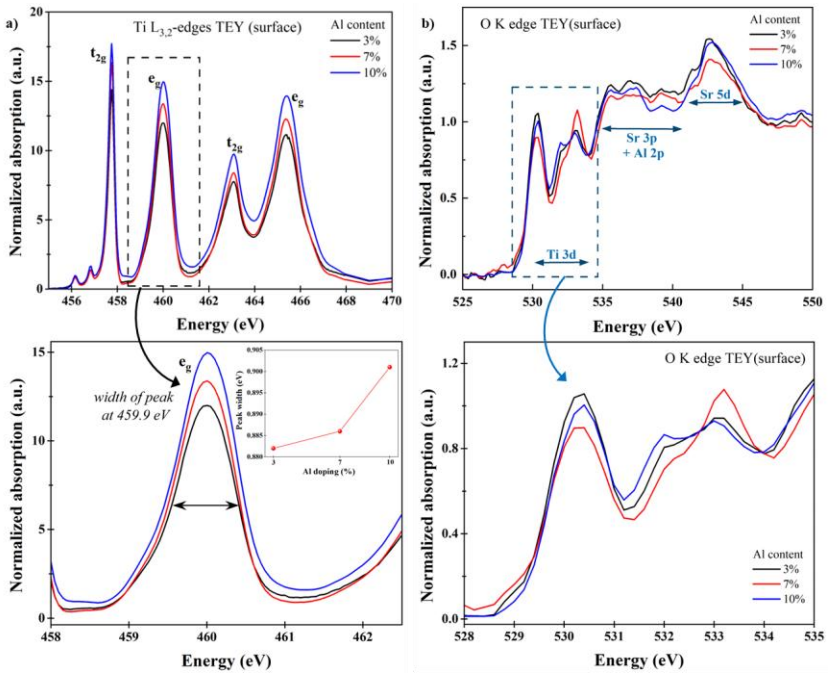

Figure IV.8. *XAS spectra recorded in TEY mode for the $L_{2,3}$ levels of Ti (a) and the K level of O (b) for the samples $Al_{3\%}$:$SrTiO_3$, $Al_{7\%}$:$SrTiO_3$ and $Al_{10\%}$:$SrTiO_3$.*

Figure IV.8b shows the X-ray absorption spectra recorded for samples of Al-doped $SrTiO_3$ in TEY mode at the oxygen K level. These reflect the hybridization of oxygen *p*-orbitals with metal states. Thus, according to the classification realized by Groot *et al.* [129], the first two peaks from 530.6 eV to 535.0 eV are assigned to hybridized Ti t_{2g} and e_g levels respectively, while the higher energy structures correspond to the hybridization with the Sr *4d*, Sr *5sp* and Ti *4sp* levels. For the sample corresponding to the 7% Al^{3+} doping, an increase in the maximum associated with the e_g component can be observed, which may be due to the formation of the SrO segregated phase, also observed in the XPS spectra in figure IV.6.

IV.2. Investigation of the photocatalytic activity of $Al_{x\%}:SrTiO_3$ materials

IV.2.1. Study of the utilization of $Al_{x\%}:SrTiO_3$ type materials for the photodegradation of Orange IV

In contrast to $SrTiO_3$, Al-doped perovskite samples show enhanced photocatalytic activity, which does not show a linear dependence on Al^{3+} content. Thus, for the sample containing 3% Al^{3+} ($Al_{3\%}:SrTiO_3$), the removal efficiency of Orange IV dye is ~88%, while for samples with higher Al^{3+} content a decrease in the efficiency of the photodegradation process is observed, reaching 65.2% ($Al_{7\%}:SrTiO_3$) and 60.8% ($Al_{10\%}:SrTiO_3$), respectively. These results indicate that the introduction of Al^{3+} into the $SrTiO_3$ structure improves photocatalytic activity, even if it does not lead to the extension of the radiation absorption range characteristic of perovskite.

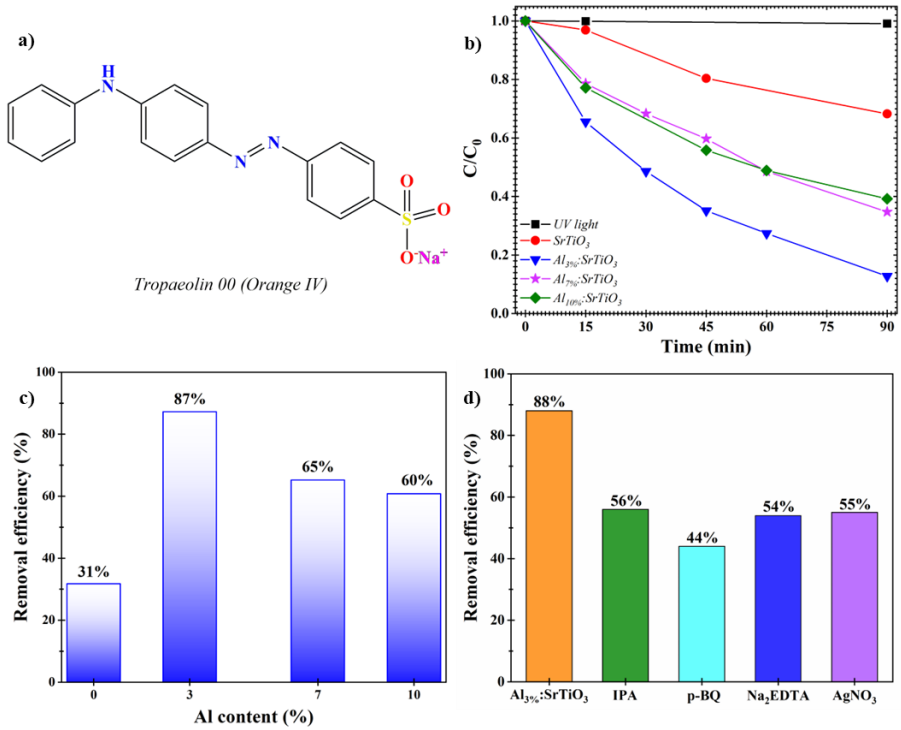

Figure IV.9. *(a) Chemical structure of Orange IV dye; (b) Graphical representation of the dye concentration evolution during the photodegradation process in the presence of different photocatalysts (c) Efficiency of the photodegradation process of Orange IV dye as a function of the amount of dopant (% Al^{3+}); (d) Efficiency of the photodegradation process of Orange IV dye in the presence of the investigated trapping agents.*

The results of the active species determination tests (fig. IV.9d) indicated that all the investigated species are involved in the photodegradation process of Orange IV dye, with a major contribution from the superoxide radicals, $O_2^{-\bullet}$, for which the photocatalytic efficiency in the presence of p-benzoquinone is reduced by half compared to the efficiency of the photocatalytic process without scavengers for the same photocatalyst.

IV.2.2. Assessment of the potential use of $Al_{x\%}$:$SrTiO_3$ materials in the photocatalytic water splitting

The efficiency of Al^{3+}-doped $SrTiO_3$ ($Al_{x\%}$:$SrTiO_3$) materials in the photocatalytic water splitting reaction was evaluated by performing photocatalytic tests which have monitored the evolution of the oxygen production reaction. Specifically, the amount of O_2 produced in the photocatalytic experiment was quantified in situ using an oxygen microsensor (miniaturized Clark-type sensor with protective cathode, Unisense).

Pure $SrTiO_3$ exhibits a very modest oxygen-producing capacity, the O_2 concentration being 1.6 μmol/L. Aluminum doping at various concentrations has a substantial impact on the photocatalytic activity. Thus, $Al_{10\%}$:$SrTiO_3$ exhibits a significant improvement in the photocatalytic efficiency of the OER reaction compared to pure $SrTiO_3$, it generates 20.89 μmol/L O_2. In contrast, both $Al_{3\%}$:$SrTiO_3$ and $Al_{7\%}$:$SrTiO_3$ show an increase in photocatalytic efficiency, but slightly lower than that recorded for $Al_{10\%}$:$SrTiO_3$, the resulting oxygen concentration being 18.83 μmol/L respectively 13.7 μmol/L.

The obtained results indicate that there is not a uniform dependence of the resulting oxygen concentration on the amount of Al^{3+}, but they correlate perfectly with the information obtained from XPS and XAS analysis of the electronic structure of the tested materials.

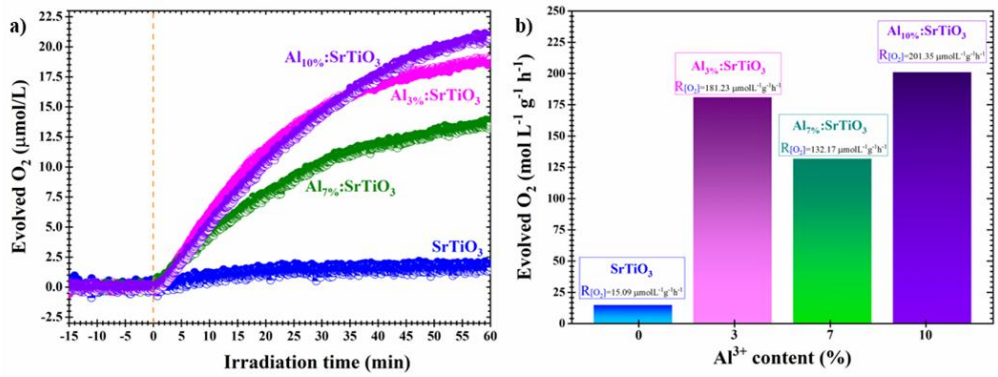

Figure IV.10. *a) Evolution of the oxygen concentration resulting from the POWS process under the action of visible light and in the presence of the photocatalysts studied: $SrTiO_3$ pure and Al^{3+} doped $SrTiO_3$; b) Comparison of the OER reaction rates.*

The introduction of aluminum into the $SrTiO_3$ structure is inevitably accompanied by the formation of oxygen vacancies and reduced Ti^{3+} species, sometimes also Ti^{2+}, to maintain the neutrality of the system. These generate defect states in the upper half of the forbidden band, which contributes to the enhanced photocatalytic performance ($Al_{3\%}$:$SrTiO_3$ case). However, the oxygen vacancies accumulate at the Al:$SrTiO_3$ surface and can act as recombination centers, therefore high concentrations of V_Os, which appears as a result of increased doping, can reduce photocatalytic activity, the case of $Al_{7\%}$:$SrTiO_3$ material. The presence of V_Os is associated with *n*-type doping of $SrTiO_3$, and the reduction of Ti^{4+} to Ti^{3+} is accompanied by the injection of two electrons: one defining localized levels in the forbidden band of $SrTiO_3$ and the other defining metallic conductivity in the form of a two-dimensional electronic system at the surface of $SrTiO_3$. For $Al_{10\%}$:$SrTiO_3$ we assume that the metallic conductivity at the surface is the critical aspect that enhances the catalytic efficiency and mitigates the effects of the other defects. This metallic state reduces the recombination of the photogenerated species and prolongs the lifetime of the individual excited states, e^- and h^+, thus favoring the concomitant development of the oxidation/reduction reactions.

V. NANOCOMPOSITES BASED ON FUNCTIONALIZED STRONTIUM TITANATE FOR PHOTOCATALYTIC APPLICATIONS

V.1.2. Morpho-structural and opto-electronic properties of the $Al_{3\%}$:$SrTiO_3$@δ-FeOOH photocatalyst

The $Al_{3\%}$:$SrTiO_3$@δ-FeOOH nanocomposite was considered the most efficient material, which is why it was further characterized and also used in various photocatalytic degradation experiments. The Rietveld refinement performed indicated the presence of the two phases in the nanocomposite as 82.3% $Al_{3\%}$:$SrTiO_3$ and 17.7% δ-FeOOH.

From figure V.3d it can be seen that the photocatalyst $Al_{3\%}$:$SrTiO_3$@-FeOOH exhibits an absorption band in the visible range, located around 500 nm, compared to the $Al_{3\%}$:$SrTiO_3$ sample (Fig. V.3a) which exhibits absorption bands only in the UV range. Thus, the E_g values obtained for the $Al_{3\%}$:$SrTiO_3$@-FeOOH nanocomposite were 1.85 eV and 1.71 eV for the direct and indirect transitions, respectively, values indicating that the $Al_{3\%}$:$SrTiO_3$@-FeOOH material exhibits photocatalytic activity under visible light radiation.

The N_2 adsorption-desorption isotherm and pore size distribution are shown in figure V.3b. According to IUPAC convention, the obtained isotherm (figure V.3b) can be classified as a type IV isotherm with type H1 hysteresis curve, which indicates the presence of pores with average pore diameter size, characteristic of the mesoporous structure. Therefore, the $Al_{3\%}$:$SrTiO_3$@δ-FeOOH nanocomposite is characterized by slit-like pores with a specific surface area of 87.98 m^2/g.

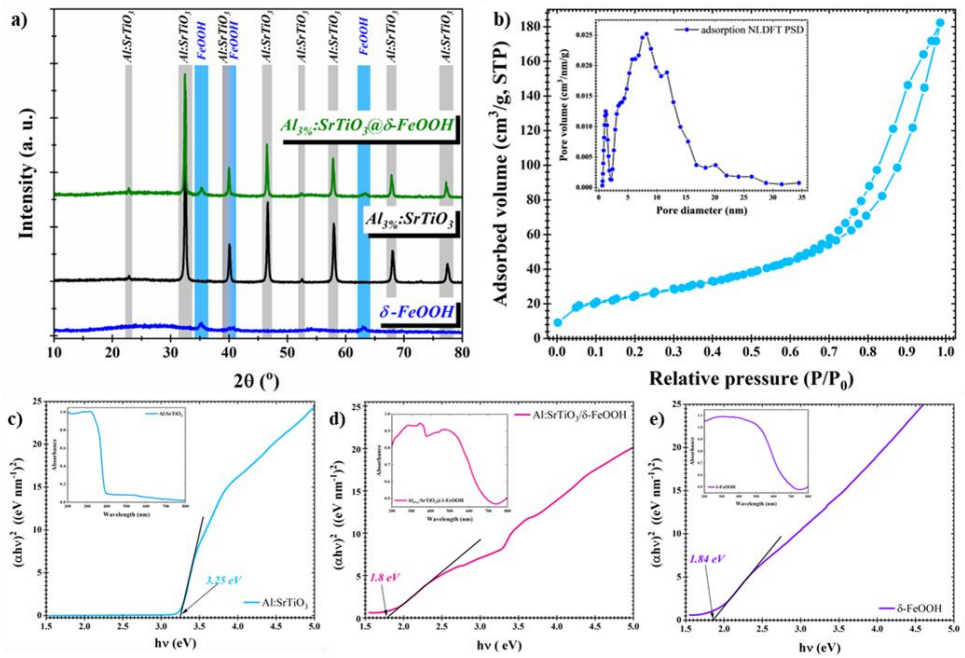

Figure V.3. *(a) Superimposed X-ray diffractograms for $Al_{3\%}$:$SrTiO_3$, δ-FeOOH and $Al_{3\%}$:$SrTiO_3$@δ-FeOOH nanocomposite; (b) N_2 adsorption-desorption isotherm corresponding to $Al_{3\%}$:$SrTiO_3$@δ-FeOOH (inset: pore diameter distribution); c-e) Tauc representations derived from UV-Vis absorption spectra for $Al_{3\%}$:$SrTiO_3$, δ-FeOOH and $Al_{3\%}$:$SrTiO_3$@δ-FeOOH.*

The FE-SEM images shown in fig. V.4(a-d) indicate the existence of $Al_{3\%}$:$SrTiO_3$ in the form of irregular and slightly agglomerated cubic particles functionalized with δ-FeOOH lamellar formations. The FE-SEM images show that the oxyhydroxide particles are not uniformly distributed on the $Al_{3\%}$:$SrTiO_3$ surface, but form clusters in which the perovskite particles are covered by the lamellar δ-FeOOH lattice. The combined and individual elemental distribution images for the $Al_{3\%}$:$SrTiO_3$@δ-FeOOH nanocomposite which are shown in fig. V.4(e-j) confirm the presence of Sr, Ti, O and Fe atoms in the nanocomposite and the uniform distribution of Al^{3+} cations on the $Al_{3\%}$:$SrTiO_3$ surface.

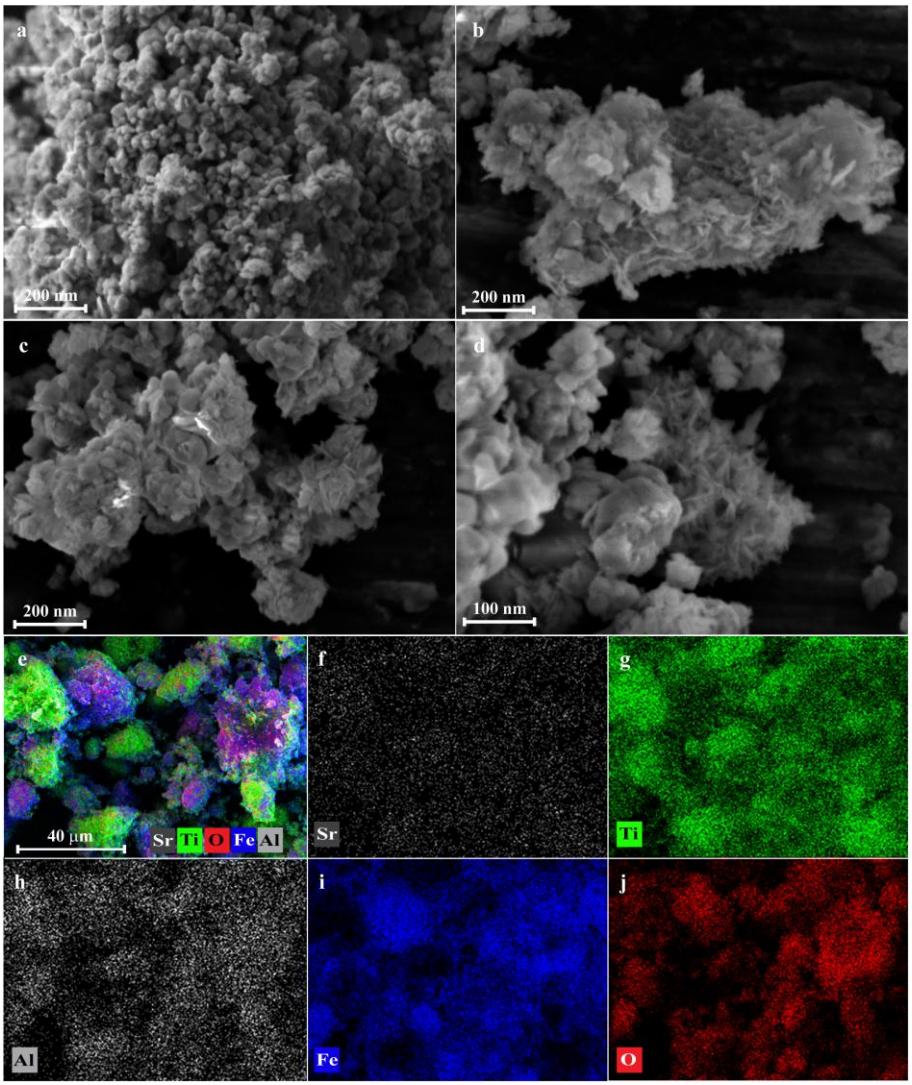

Figure V.4. *FE-SEM images at different magnifications highlighting the morphology of the nanocomposite $Al_{3\%}$:$SrTiO_3$@δ-FeOOH (a) and images showing the combined elemental distribution (e) as well as the individual distribution (f-j) of the atoms in the nanocomposite composition.*

Figure V.5 shows the XPS spectra of Ti *2p* and O *1s* recorded for $Al_{3\%}$:$SrTiO_3$ and $Al_{3\%}$:$SrTiO_3$@δ-FeOOH under vacuum conditions and in the presence of water vapor. The individual Ti *2p* spectra for the two samples under the given conditions are shown in figure V.6. In the corresponding Ti *2p* spectra, the presence of additional signatures accompanying the main valence of titanium, Ti^{4+}, was mainly followed.

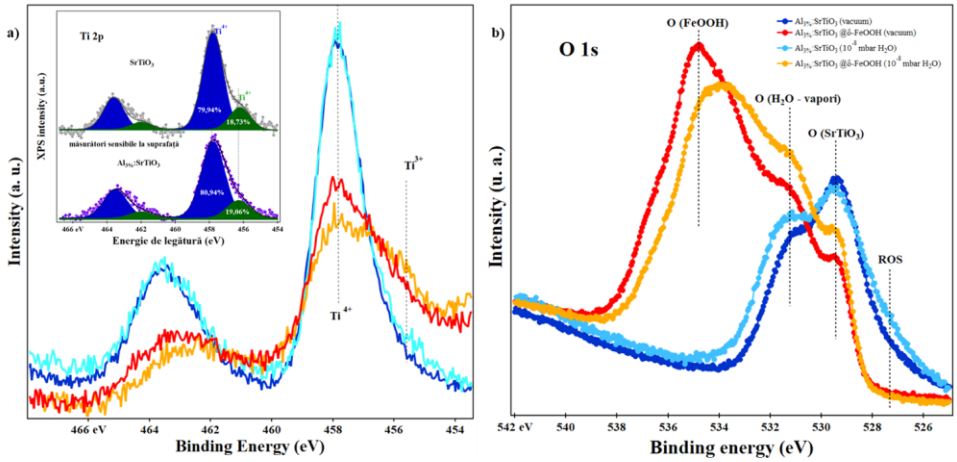

Figure V.5. *XPS spectra of Ti 2p (a) and O 1s (b) recorded for $Al_{3\%}$:$SrTiO_3$ and $Al_{3\%}$:$SrTiO_3$@δ-FeOOH under high vacuum conditions and in the presence of water vapors.*

From figure V.5, in addition to the attenuation of the titanium signal due to the formation of the $AlO_x/SrTiO_3$ interface, it can be observed that the ratio of the Ti^{3+}/Ti^{4+} components intensities is different in $Al_{3\%}$:$SrTiO_3$ compared to $Al_{3\%}$:$SrTiO_3$@δ-FeOOH. This aspect indicates that under the FeOOH layer, the presence of Ti^{3+} species increases, thus leading to the concomitant formation of oxygen vacancies, V_Os.

The combined XPS spectra of O *1s* (fig. V.5b) and individual spectra simulated with Voight lines (Fig. V.7) reflect both the spectral signature of oxygen in the perovskite lattice environment located at ~529 eV and the oxygen signature from FeOOH at ~535 eV.

The variation of the Ti^{3+}/Ti^{4+} ratio is accompanied by the presence of the constant signal generated by Al 2p in $Al_{3\%}$:$SrTiO_3$ (fig. V.7(a-c)) irrespective of the analysis conditions, which, however, changes for the $Al_{3\%}$:$SrTiO_3$@δ-FeOOH system. Specifically, as can be seen from fig. V.8b, under vacuum conditions, the metallic component of aluminum increases in $Al_{3\%}$:$SrTiO_3$@δ-FeOOH, whereas, during exposure to UV light and water (V.8d), it decreases drastically.

Figure V.9a shows the X-ray absorption spectra recorded, in TEY mode, of the Fe $L_{2,3}$ edges for the sample $Al_{3\%}$:$SrTiO_3$@δ-FeOOH which is almost identical to the corresponding spectrum of δ-FeOOH oxyhydroxide, demonstrating that

δ-FeOOH is present on the surface region. Moreover, the TFY Fe L-edge spectra for the $Al_{3\%}$:$SrTiO_3$@δ-FeOOH and δ-FeOOH are also identical, which proves that FeOOH is not mixed into the $SrTiO_3$ core particles. For $Al_{3\%}$:$SrTiO_3$, the amplitude of the absorption maximum characteristic of the Ti $L_{2,3}$ edges (fig. V.9c) is higher than that measured for the $Al_{3\%}$:$SrTiO_3$@δ-FeOOH sample due to the FeOOH layer on the surface, which hinders the expulsion of photoelectrons and reduces the TEY signal.

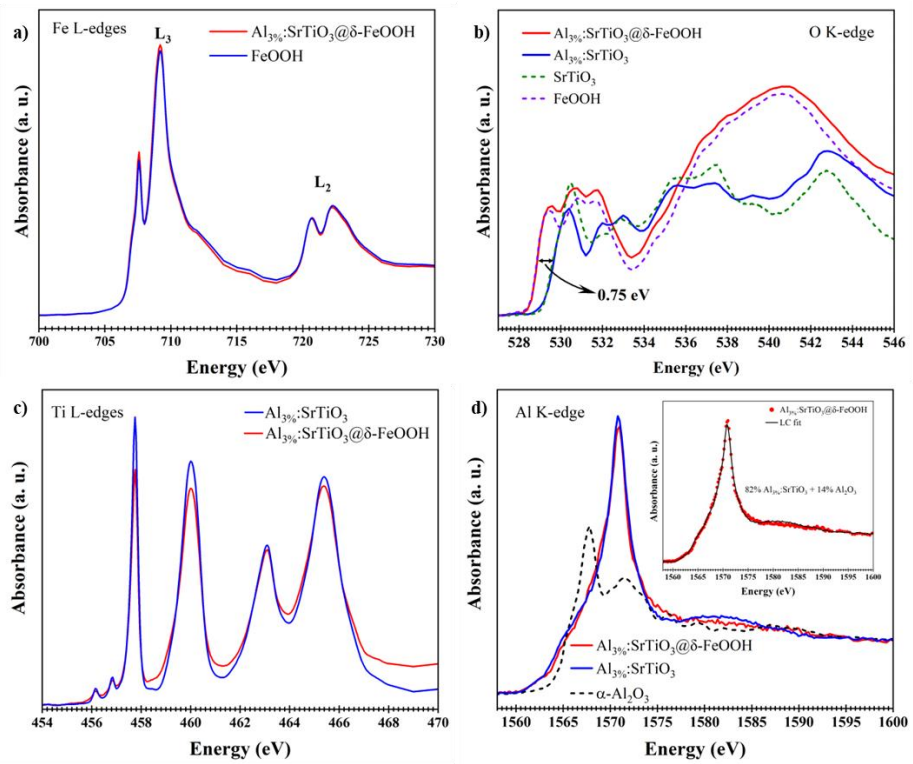

Figure V.9. *XAS spectra of: $L_{2,3}$ Fe levels for $Al_{3\%}$:$SrTiO_3$@δ-FeOOH and FeOOH (reference) in TEY mode (a); K a O levels for $Al_{3\%}$:$SrTiO_3$@δ-FeOOH compared to $Al_{3\%}$:$SrTiO_3$ and with reference $SrTiO_3$ and FeOOH, (dashed lines) in TEY mode (b); $L_{2,3}$ levels of Ti for $Al_{3\%}$:$SrTiO_3$@δ-FeOOH and $Al_{3\%}$:$SrTiO_3$, in TEY mode (c); K a Al levels for $Al_{3\%}$:$SrTiO_3$@δ-FeOOH, in TFY, and reference Al_2O_3, in TEY (d).*

For the $Al_{3\%}$:$SrTiO_3$@δ-FeOOH nanocomposite, the XAS spectrum for the oxygen K-level (Fig. V.9b) is comparable to that of FeOOH and shows a 0.75 eV shift to lower energies, which is consistent with the band gap reduction shown in fig. V.3c. The spectrum for the K level of aluminum measured in TFY which is

illustrated in Figure V.9d, it indicates the existence of a dominant $Al_{3\%}$:$SrTiO_3$ feature (82%), but also a contribution from Al_2O_3 (14%), most likely localized at the surface.

V.1.3. Investigation of the photocatalytic activity of Al3%:SrTiO3@δ-FeOOH in the photodegradation process of Orange IV

In order to determine the optimum pH for the photodegradation reaction of Orange IV dye, photocatalytic experiments were carried out at different pH values of the dye solution (1.5; 7 and 12). The results of these experiments, which are shown in figure V.10a, suggest that the photodegradation of the dye occurs only at acidic pH of the solution. This experimental aspect is also supported by the results obtained on the determination of the isoelectric point of the material $Al_{3\%}$:$SrTiO_3$@δ-FeOOH, whose value is 7.1 (Fig. V.10b).

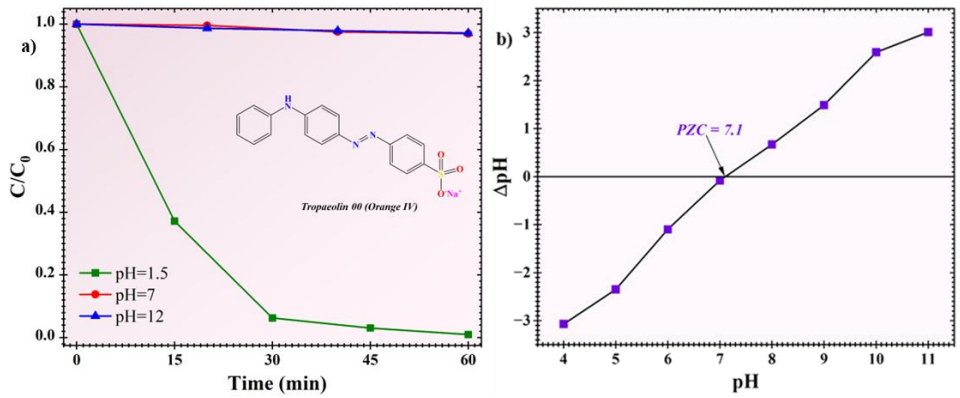

Figure V.10. *a) Influence of solution pH on the photodegradation process of Orange IV dye; b) Determination of the isoelectric point of $Al_{3\%}$:$SrTiO_3$@δ-FeOOH nanocomposite.*

From figure V.11a it can be seen that the impact of visible radiation on the dye solution is insignificant, with only 1.4% of the dye solution being degraded after 60 minutes of irradiation. Concerning the use of δ-FeOOH as photocatalyst in the dye degradation process, the obtained results (Fig. V.11a) indicated that 75% of the dye molecules were degraded after 60 minutes of irradiation, whereas, the use of $Al_{3\%}$:$SrTiO_3$@δ-FeOOH nanocomposite leads to almost total degradation of the dye solution (≈99%).

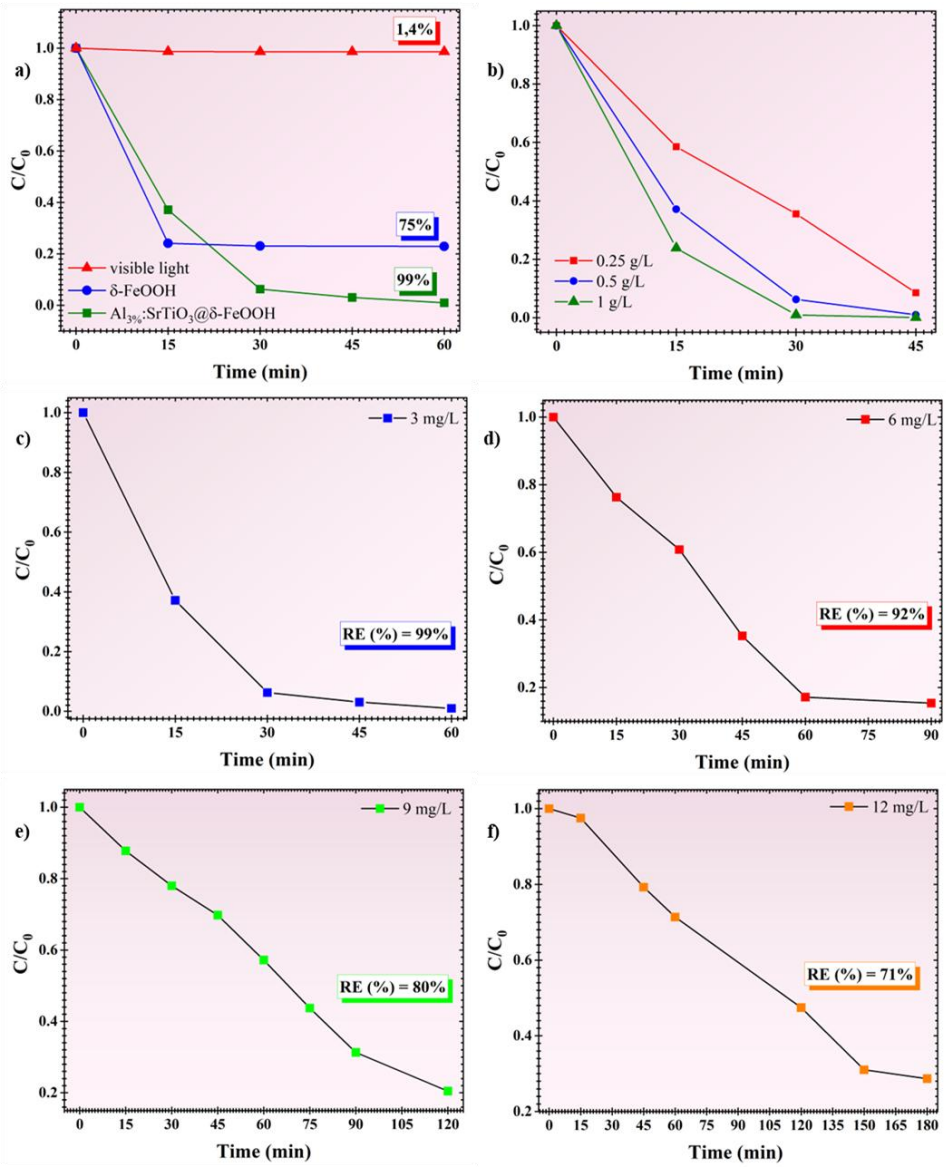

Figure V.11. *a) Comparison between the efficiency of the photodegradation process of Orange IV dye using VIS radiation, δ-FeOOH and $Al_{3\%}$:$SrTiO_3$@δ-FeOOH as photocatalysts; b) Influence of photocatalyst concentration on the efficiency of the photodegradation process of Orange IV dye; (c-f) Influence of dye solution concentration on the efficiency of the photocatalytic process.*

The influence of the photocatalyst concentration on the photodegradation process of Orange IV dye was evaluated by performing photocatalytic tests using different concentrations of photocatalyst, namely 0.25 g/L, 0.5 g/L and 1 g/L. Thus, the results obtained (fig. V.11b) show that there are no significant differences

between the photocatalyst efficiency values, which is over 90% after 60 minutes of irradiation, for all three concentrations tested.

From fig. V.12a-b it can be seen that after three degradation cycles, the photocatalyst maintains its photocatalytic activity, the photodegradation process efficiency is over 90%. This aspect suggests that the $Al_{3\%}$:$SrTiO_3$@δ-FeOOH photocatalyst is reusable and can be used in multiple photocatalytic cycles. From the X-ray diffractograms (fig. V.12b) of the photocatalyst before and after the photocatalytic experiment, it can be observed that no reflections specific to other structures than the existing ones ($SrTiO_3$ and δ-FeOOH) appear. Therefore, it can be stated that the photocatalyst, $Al_{3\%}$:$SrTiO_3$@δ-FeOOH is stable and does not undergo structural changes during the irradiation process.

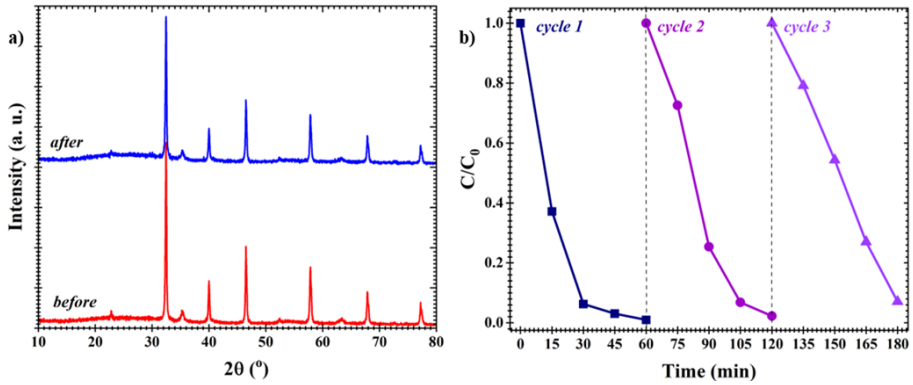

Figure V.12. *a) The photocatalytic efficiency of $Al_{3\%}$:$SrTiO_3$@δ-FeOOH nanocomposite in the photocatalytic degradation process of Orange IV dye after three cycles of use; b) X-ray diffractograms recorded for $Al_{3\%}$:$SrTiO_3$@δ-FeOOH photocatalyst before and after the photocatalytic process.*

V.1.3.2. Proposed mechanism for the photocatalytic degradation of Orange IV dye in the presence of the photocatalyst $Al_{3\%}$:$SrTiO_3$@δ-FeOOH

The results of the photodegradation experiments carried out in the presence of the above-mentioned trapping agents are shown in figure V.13a. The decrease in photocatalytic efficiency in the presence of p-benzoquinone indicates that $O_2^{\bullet-}$ radicals play an important role in the photocatalytic process, as they are directly responsible for the degradation of Orange IV dye in the presence of the nanocomposite $Al_{3\%}$:$SrTiO_3$@δ-FeOOH.

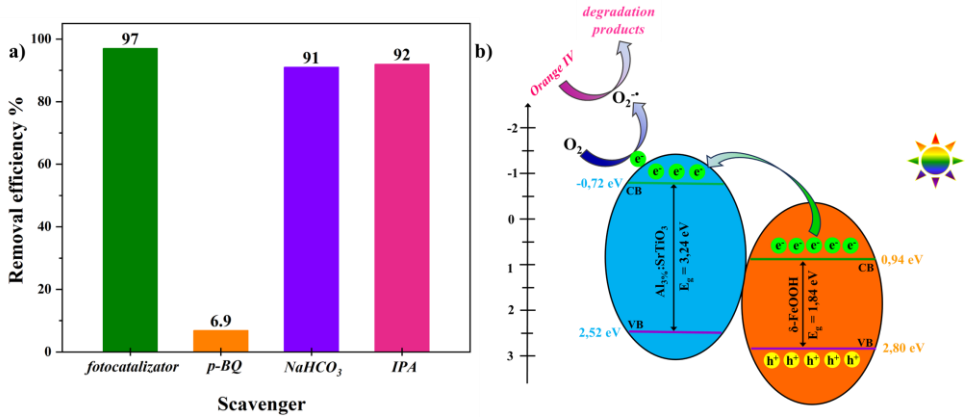

Figure V.13. *a) The efficiency of the photodegradation process of Orange IV dye in the presence of the investigated trapping agents; b) The proposed mechanism of the photocatalytic degradation process of Orange IV dye in the presence of the photocatalyst* $Al_{3\%}$*:*$SrTiO_3$*@δ-FeOOH under the action of visible light.*

The alignment of the electronic bands with respect to the values obtained for their potentials indicates the formation of a type II heterojunction. Following irradiation with visible radiation, electrons in the valence band of the oxyhydroxide (FeOOH) are excited and migrate into its conduction band, forming gaps in the valence band. Subsequently, the excited electrons will be transferred to the conduction band of perovskite ($Al_{3\%}$:$SrTiO_3$) where they will react with adsorbed O_2 molecules leading to the formation of superoxide radicals. The potential of the conduction band for δ-FeOOH is lower (more positive) than the potential for $O_2/O_2^{-\bullet}$ reduction (-0.33 eV) indicating that the O_2 reduction reaction with $O_2^{-\bullet}$ formation will not occur in the conduction band of FeOOH. Normally, the remaining voids in the valence band of FeOOH could either participate in the HO- radical formation reaction or interact directly with the dye molecules causing its degradation. In the present case, although the valence band potential of δ-FeOOH, which is higher than the $HO^{\bullet}$ radical formation potential (H_2O/ $HO^{\bullet}$ - 2.4 eV vs. NHE), suggests that the accumulated voids could oxidize H_2O molecules to form hydroxyl radicals, experiments performed to determine the active species did not indicate the presence of $HO^{\bullet}$ radicals.

V.1.4. Investigation of the photocatalytic activity of $Al_{3\%}$:$SrTiO_3$@δ-FeOOH in the photodegradation process of Tetracycline

As can be seen from figure V.15b, tetracycline, in solution, shows high stability, the percentage of tetracycline degraded after 48 h (due to the self-degradation process) being insignificant (less than 1%). In comparison, the effect of radiation on the tetracycline solution was significant, 50% of the initial concentration of the antibiotic solution being degraded after 80 min of irradiation. The presence of the photocatalyst causes a sharp decrease in the concentration of tetracycline to almost zero concentration (total degradation) of tetracycline, the efficiency of the photodegradation process being 97% after 75 minutes of irradiation.

Figure V.15c-f shows the results of the photocatalytic experiments for all concentrations investigated, suggesting that the performance of the photocatalyst is not influenced by the initial concentration of antibiotic solution used. Thus, for all the three concentrations studied, the efficiency of the degradation process is more than 95% after the 75 minutes of irradiation, the differences obtained for the values of the rate constants associated with the corresponding photocatalytic reactions being insignificant. The efficiency of the nanocomposite in the photocatalytic degradation process of the studied antibiotic can be observed in the chromatograms obtained for each tested solution (fig. V.15d-f), chromatograms in which a gradual decrease in the area of the chromatographic signal associated with tetracycline is observed with increasing irradiation time.

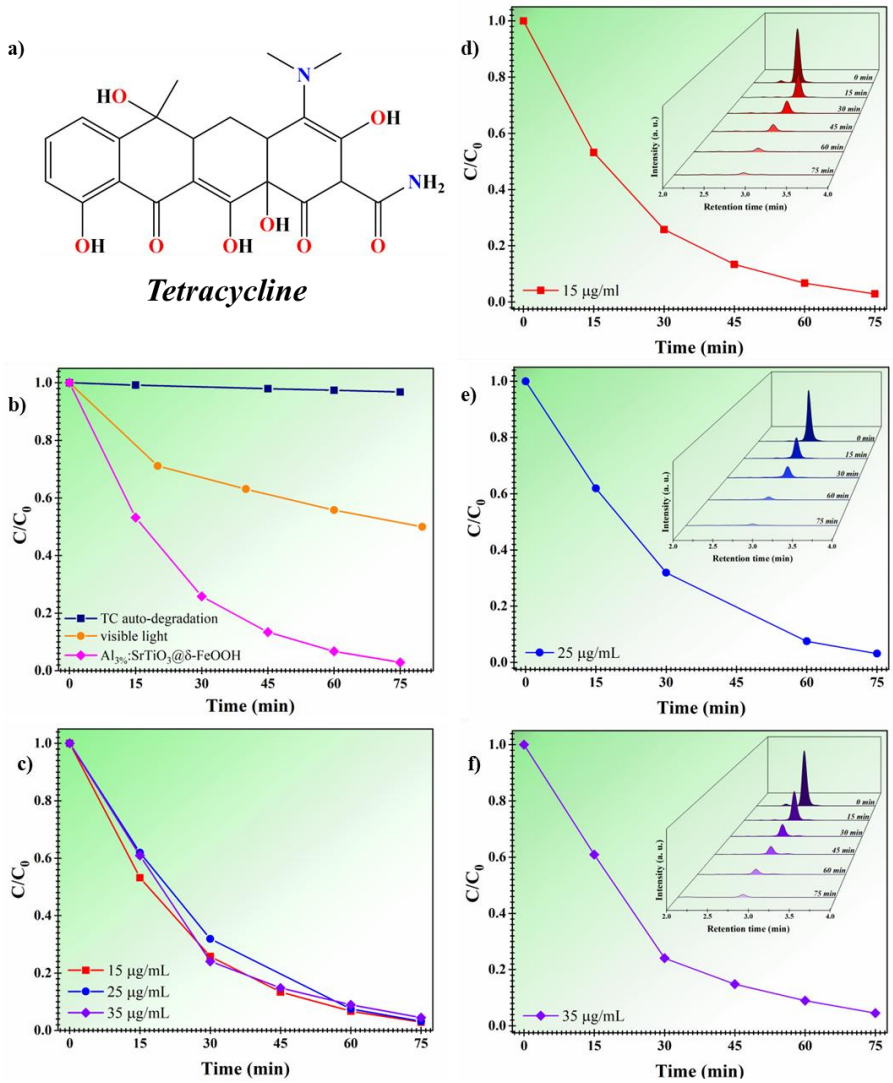

Figure V.15. *Structure of tetracycline (a); Evolution of tetracycline concentration over time for the three processes: auto-degradation, photolysis and photocatalytic degradation in the presence of $Al_{3\%}$:$SrTiO_3$@δ-FeOOH (b); Comparative evolution of tetracycline concentration during the photocatalytic process for the three concentrations (c) and individual evolution of tetracycline concentration (d-f).*

Identification possible degradation products and proposing a mechanism for tetracycline degradation

Based on the experimental results obtained from HPLC-MS analysis and in accordance with the literature [147-150], a degradation mechanism of tetracycline was proposed, which is shown in Figure V.18.

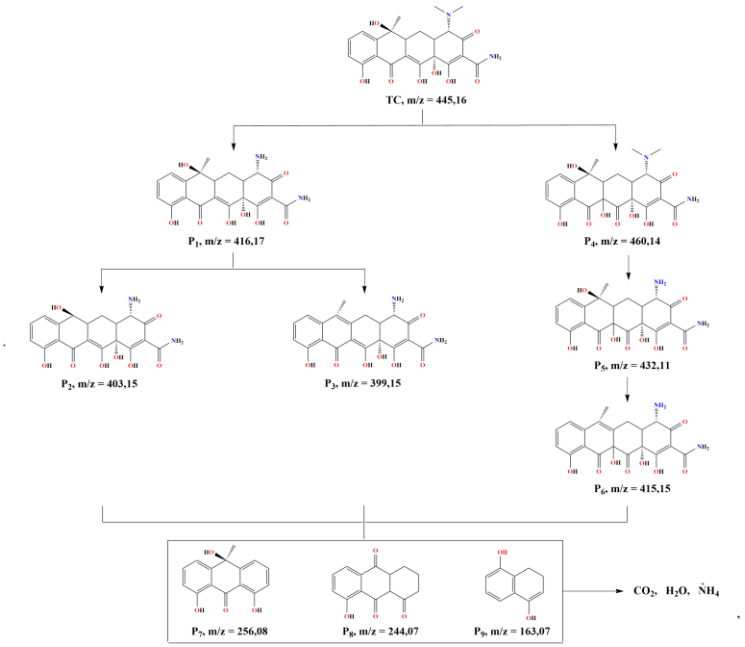

Figure V.18. *Proposed mechanism for the photocatalytic degradation of tetracycline under the action of visible radiation using $Al_{3\%}$:$SrTiO_3$@δ-FeOOH photocatalyst.*

Thus, the N-demethylation process of tetracycline occurs under the action of the holes (h^+) formed in the valence band of the photocatalyst, resulting in the intermediate P_1 (m/z=416). This, by successive demethylation at the carbon atom (C_8), forms the intermediate P_2 (m/z=403), and by the action of superoxide radicals on the P_1 intermediate, the intermediate P_3 (m/z=399) is obtained. In parallel, as a result of attack by hydroxyl radicals ($HO^{\bullet}$), tetracycline (TC, m/z=445) molecules undergo hydroxylation, resulting in the formation of intermediate P_4 (m/z=460), which subsequently, under the action of vacancies, removes the N-$(CH_3)_2$ group, leading to the appearance of intermediate P_5 (m/z=432). The P_6 intermediate (m/z=415) is obtained by oxidation of the P_5 intermediate by superoxide radicals, $O_2^{-\bullet}$. Further, under the action of holes and $O_2^{-\bullet}$ radicals, intermediates P_1-P_6 undergo various transformations, such as deamination, dealkylation, carbonyl elimination, oxidation and ring opening, leading to the formation of intermediates P_7-P_9 (m/z=256, m/z=244, m/z=163). As the photocatalytic reaction proceeds, through

oxidative processes, these are transformed into smaller organic molecules, which can subsequently be mineralized into simple molecules such as CO_2, H_2O or $^+NH_4$.

V.2. Cobalt oxyhydroxide (CoOOH) coating on $Al_{3\%}$:$SrTiO_3$ surface

Although in the diffractogram of the nanocomposite (fig. V.19a), the intensity of the CoOOH phase-specific reflections at 19.75°, 36.45°, 39.11°, 50.71° and 65.30° is very low compared to the intensity of the perovskite-specific reflections, they allowed Rietveld refinement to identify the constituent phases of the nanocomposite. The two phases were indexed using the references ICSD 98-009-1899 for the perovskite phase and ICSD 98-001-2587 for the oxyhydroxide phase, and they are found in the nanocomposite in the proportion of 92.7% $Al_{3\%}$:$SrTiO_3$ and 7.3% CoOOH, respectively.

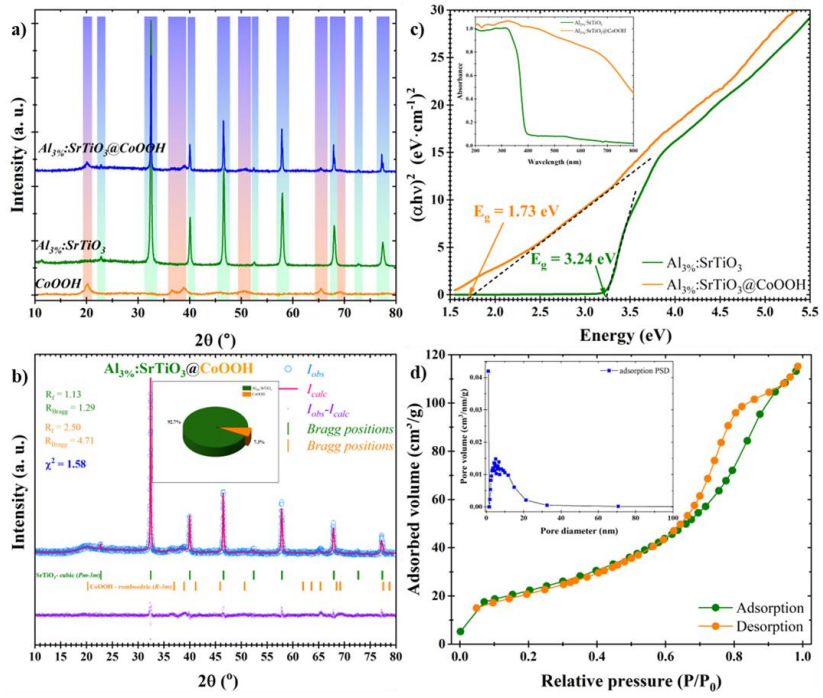

Figure V.19. *a) Superimposed X-ray diffractograms recorded for $Al_{3\%}$:$SrTiO_3$, CoOOH and $Al_{3\%}$:$SrTiO_3$@CoOOH nanocomposite; b) Rietveld refinement performed on the corresponding nanocomposite diffractogram and the percentage of phases; c) Tauc representations corresponding to the UV-Vis absorption spectra; d) N_2 adsorption-desorption isotherm recorded for the nanocomposite $Al_{3\%}$:$SrTiO_3$@CoOOH and pore size distribution.*

The UV-Vis absorption spectrum (fig. V.19c) recorded for the $Al_{3\%}$:$SrTiO_3$@CoOOH nanocomposite shows a new absorption maximum around 700 nm, which confirms that the development of a nanocomposite by coupling two semiconductors is a promising strategy to extend the light absorption range of $SrTiO_3$. The adsorption-desorption isotherm of N_2 (Fig. V.19d) recorded for the $Al_{3\%}$:$SrTiO_3$@CoOOH nanocomposite indicates the existence of a mesoporous material, characterized by large adsorption specific surface area of 80.86 m^2/g. The FE-SEM images shown in Figure V.20 highlight the presence of $Al_{3\%}$:$SrTiO_3$ perovskite in the form of polyhedral, multifaceted particles, while CoOOH oxyhydroxide is characterized by thin particles with irregular lamellar shape, randomly distributed throughout the sample volume.

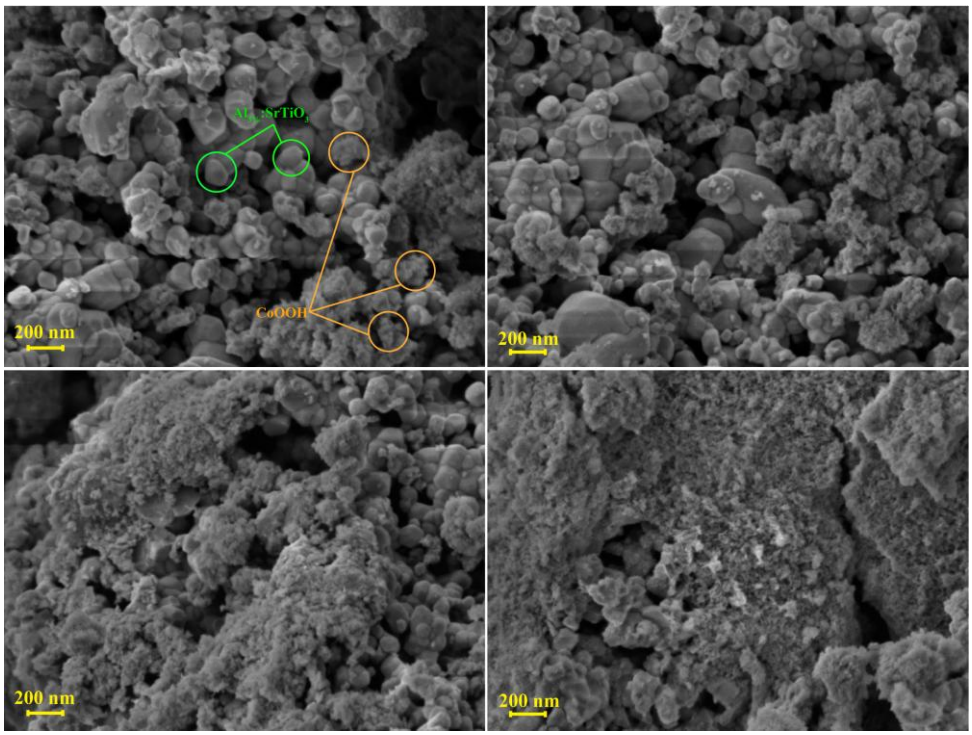

Figure V.20. *FE-SEM images of $Al_{3\%}$:$SrTiO_3$@CoOOH nanocomposite at different magnifications.*

XPS analysis results confirm the presence of CoOOH in the composition of the $Al_{3\%}$:$SrTiO_3$@CoOOH nanocomposite by the intense signal identified in fig. V.21a, which coincides with that simulated in fig. V.21b. The main Co *2p*

maximum, which occurs at 780.6 eV, indicates that 87% of the cobalt ions are in the +3 oxidation state (Co^{3+}), and the difference corresponds to cobalt ions in the higher oxidation state [151]. The $SrTiO_3$ surface is close to the expected stoichiometry of 1:1 between Ti and Sr (fig. V.21c-d), with the titanium cations exhibiting the ideal valence, Ti^{4+}, in octahedral symmetry.

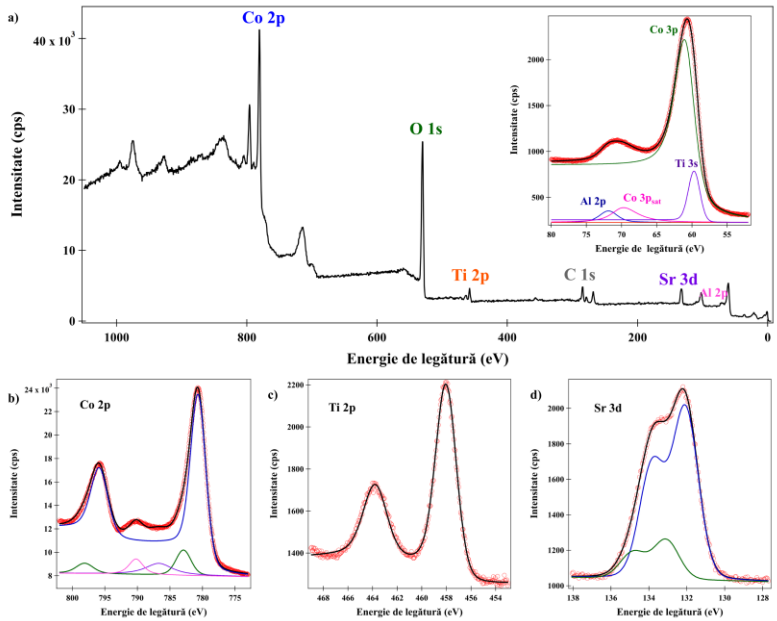

Figure V.21. *Survey XPS spectrum of the nanocomposite $Al_{3\%}$:$SrTiO_3$@CoOOH, showing the main characteristic lines (a); XPS spectra for Co 2p (b), Ti 2p (c) and Sr 3d (d) with simulated Voight lines.*

The corresponding Al 2p maximum, obtained by its deconvolution from the Co *3p* and Ti *3s* contributions, is located at 72.1 eV and indicates the presence of a significantly lower state, but not totally up to the metallic state (Al^0), the metallic contribution being normally present at 72.7 eV [152].

V.2.2. Evaluation of the photocatalytic activity of $Al_{3\%}$:$SrTiO_3$@CoOOH in the oxacillin degradation process

Figure V.22a shows the comparative efficiency of the oxacillin degradation process using different concentrations of the photocatalyst $Al_{3\%}$:$SrTiO_3$@CoOOH (0.25 g/L; 0.5 g/L and 1 g/L). Thus, in the absence of the photocatalyst, but under the action of light in the visible range (photolysis process), the degradation of

oxacillin is negligible (< 1%), suggesting that under the action of light, oxacillin is stable and the following results obtained are due to the activity of the photocatalyst. For the photocatalyst concentration of 1 g/L in the dark at equilibrium, 90% of the oxacillin molecules in the initial solution (10 µg/mL) were adsorbed on the surface of the $Al_{3\%}$:$SrTiO_3$@CoOOH nanocomposite. Also, the amount of oxacillin adsorbed at equilibrium decreases with decreasing photocatalyst concentration, which can be attributed to the lower number of available active centers. Thus, the photocatalytic efficiency decreases from 99% for the concentration of 1 g/L $Al_{3\%}$:$SrTiO_3$@CoOOH to 78% and 44% for 0.5 g/L and 0.25 g/L, respectively. This aspect highlights the importance and complementarity of the adsorption and degradation steps during the photocatalytic process [157]. For all the concentrations of photocatalyst, respectively, antibiotic tested, the photocatalytic degradation process of oxacillin is described by the pseudo-first order kinetic model.

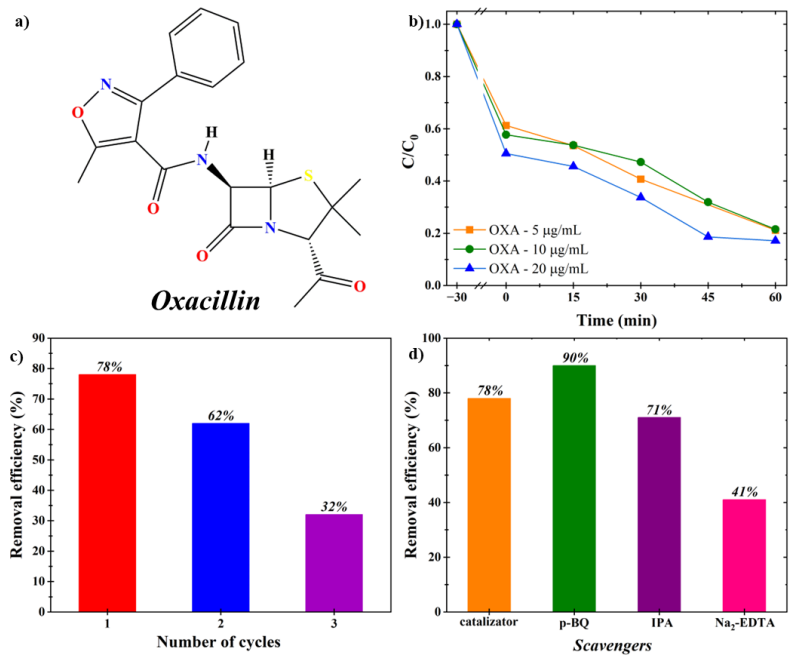

Figure V.23. *a) Chemical structure of oxacillin; b) C/C0 vs time representations corresponding to the photodegradation processes in the presence of the photocatalyst $Al_{3\%}$:$SrTiO_3$@CoOOH, as a function of the initial concentration of the oxacillin solution; c) reusability of the $Al_{3\%}$:$SrTiO_3$@CoOOH after three cycles of use (0.5 g/L photocatalyst, 10 µg/mL OXA); d) the result of tests for the determination of reactive species responsible for oxacillin photodegradation in the presence of $Al_{3\%}$:$SrTiO_3$@CoOOH nanocomposite (10 µg/mL OXA and 0.5 g/L photocatalyst).*

Figure V.23b shows that the efficiency of the photocatalytic degradation process after 60 minutes of irradiation is about 80%, regardless of the initial concentration of the antibiotic solution. These results indicate that the $Al_{3\%}$:$SrTiO_3$@CoOOH photocatalyst is also active at higher concentrations of antibiotic solution, the photocatalytic activity is not influenced by the initial antibiotic concentration. They also suggest that the efficiency of the photocatalytic process is rather due to the microstructural properties and high adsorption capacity of the photocatalyst. By associating the two processes, adsorption and photodegradation act synergistically for the degradation of the studied antibiotic.

The tests performed to evaluate the reusability of the $Al_{3\%}$:$SrTiO_3$@CoOOH photocatalyst were carried out without reactivating the photocatalyst. Thus, the results obtained indicated a decreasing trend in the efficiency of the photocatalyst (fig. V.23c) with increasing number of photocatalytic cycles in which it is used, from 78% to 32%, suggesting that the photocatalyst loses its efficiency under these conditions of use. This decrease in efficiency can be attributed to the number of available active centers, which is decreasing when the photocatalyst is not reactivated.

The results of the determination tests (fig. V.23d) show that the addition of isopropanol (IPA) has an insignificant influence on the photocatalytic efficiency, thus suggesting that hydroxyl radicals ($HO^{\bullet}$) are not involved in the photocatalytic reaction. In contrast to $HO^{\bullet}$ radicals, in the case of vacancies, the addition of Na_2-EDTA led to decreased photocatalytic efficiency, indicating that vacancies are the main active species responsible for the photocatalytic degradation of oxacillin in the presence of $Al_{3\%}$:$SrTiO_3$@CoOOH nanocomposite and under the action of visible-range radiation. In addition, when *p*-BQ was added to the reactor, an increase in the photocatalytic efficiency was observed, indicating that the superoxide radicals $O_2^{-\bullet}$ facilitate the photocatalytic reaction.

GENERAL CONCLUSIONS

Oxide nanomaterials constitute a category of materials of particular importance in the field of nanomaterials, which are being intensively studied for their use as photocatalysts in topical photocatalytic applications, such as the removal of contaminants from water or the production of H_2 by photocatalytic decomposition of water, but also for use in other types of applications.

In the first part of the thesis, theoretical aspects about the structure of oxide nanomaterials with spinel and perovskite-type structure were presented, as well as information extracted from the literature on the synthesis methods of these materials, the characterization techniques used and their applications.

The first study in the experimental part of the thesis presented the synthesis and characterization of Zn-Mn mixed ferrite nanoparticles substituted with Gd^{3+} ions, $Zn_{0.7}Mn_{0.3}Fe_{2-x}Gd_xO_4$ (x = 0; 0.025; 0.050; 0.075; 0.100), which were subsequently tested for their use as photocatalysts for rhodamine degradation, as well as for their use as sensors for acetone. Analysis of the obtained results led to the following conclusions:

- X-ray diffraction analysis confirmed that the desired spinel structure was obtained for all five compositions, corresponding to the two heat treatments applied. However, for the ones sintered at 650 °C, in addition to the cubic spinel phase, secondary phases were observed due to the presence of bulky Gd^{3+} ions, which tend to leave the lattice at higher temperatures.
- Ferrite samples obtained at 500 °C are presented as spherical, agglomerated nanoparticles in the size range 20-30 nm and exhibit superparamagnetic behavior.
- The photocatalytic activity of single and Gd^{3+} ion-doped ferrite samples heat treated at 500 °C and 650 °C, respectively, was evaluated by performing photodegradation tests of rhodamine B under the action of visible light.

- The obtained results showed that the materials exhibit photocatalytic activity under the action of visible radiation, the photocatalytic degradation efficiency of rhodamine, under the tested conditions, being over 80% after 180 minutes of irradiation.

- UV-Vis spectra recorded for the dye solution at different time intervals showed, for some samples tested, changes in the course of the photocatalytic reaction after the first 120 minutes of irradiation. On the basis of the UV-Vis and fluorescence spectra recorded, the observed changes, i.e., the formation of a new absorption maximum and the fluorescence change were associated with the structural transformation of rhodamine B into its derivative Rh 110. The process of rhodamine deethylation is induced by visible radiation and occurs as a result of the long irradiation time required for photocatalytic degradation of rhodamine B

- During the photocatalytic process, initially the degradation of the chromophore in the structure of Rhodamine B takes place via the active species resulting from the irradiation of the photocatalyst. In parallel, due to the long irradiation time required for its complete decomposition, part of the Rhodamine molecules is directly sensitized by light in the visible range and subsequently act on the photocatalyst, resulting in the breaking of C_{alif} - N bonds in the Rhodamine structure.

- The results of the acetone detection tests suggested that the tested materials can be used as sensors for acetone. Although the highest sensitivity value was obtained for the sample corresponding to the degree of substitution, x = 0.100 Gd^{3+}, both sensitivity and relaxation times are not influenced by some physical characteristics such as porosity or adsorption surface area and not by compositional variations. Acetone detection tests, performed at room temperature, showed that the materials exhibit good responses, comparable with other measurements reported in the literature at the same temperature.

The second study in the thesis focused on the doping of $SrTiO_3$ with Al^{3+} cations as an effective method to enhance the photocatalytic activity of perovskite.

It is essential to elucidate the relationship between dopant position, electronic structure and photocatalytic activity. Evaluation of the photocatalytic activity of $Al_{x\%}$:$SrTiO_3$ materials was carried out by performing photodegradation experiments of Orange IV dye, as well as photocatalytic water decomposition experiments.

- The Al^{3+} doped $SrTiO_3$ materials were synthesized by the ceramic method using an Al content in the range of 1-10%, and the characteristic $SrTiO_3$ cubic perovskite structure was confirmed by X-ray diffraction analysis. Based on the results obtained from XRD measurements, three of the doped samples ($Al_{x\%}$:$SrTiO_3$, x = 3, 7 and 10) were selected for detailed electronic structure analysis.

- XPS spectroscopy suggested that the doped $SrTiO_3$ samples are mostly characterized by Ti^{4+} species (ideal octahedral surround), but a contribution from Ti^{3+} and Ti^{2+} species was also observed, most frequently, these were associated with the presence of oxygen vacancies (V_{OS}). The presence of Ti^{2+} species was only observed for the sample corresponding to the highest doping percentage, $Al_{10\%:}SrTiO_3$, for which the XPS spectra recorded for Sr 3d indicated the occurrence of a component corresponding to strontium oxide, which will act as a defect and affect the photocatalytic activity. The materials exhibit surface nonstoichiometry, a deviation from the ideal Sr:Ti:O ratio (1:1:3), indicating oxygen deficiency and n-type doping with free electrons.

- The XAS spectra show that the aluminum atoms show octahedral symmetry in volume, with a significant deformation of the $Al_{7\%}$:$SrTiO_3$ sample.

- The doping of strontium titanate with Al^{3+} did not result in a reduction of the E_g value and consequently in a change of the light absorption range.

- In order to evaluate the impact of the doping process on the photocatalytic activity of $SrTiO_3$, photocatalytic degradation tests of Orange IV dye under UV radiation were performed. The efficiency of the photocatalytic degradation process of Orange IV dye performed using Al doped materials was higher than $SrTiO_3$.

These results show that the doping of $SrTiO_3$ with aluminum is an effective method to improve the photocatalytic activity of perovskite, even if it does not result in the extension of the absorption range.

- The highest photodegradation process efficiency value was obtained for the $Al_{3\%}$:$SrTiO_3$ material. For the other doped samples, a decrease in photocatalytic efficiency was observed, but still higher than that of pure $SrTiO_3$.
- Photocatalytic water decomposition experiments confirmed that the doped materials exhibit improved photocatalytic efficiency compared to pure $SrTiO_3$. They indicated an increase in the resulting oxygen concentration from 1.6 μmol/L ($SrTiO_3$) to 18.83 μmol/L ($Al_{3\%}$:$SrTiO_3$).
- The results obtained from the photocatalytic experiments carried out showed a strong correlation between the photocatalytic activity of the doped materials, their electronic structure and the changes induced by Al^{3+} doping.

The aim of the third study was to develop Al^{3+}-doped $SrTiO_3$-based photocatalysts that are active under the action of visible radiation by depositing another semiconductor on the perovskite surface. The deposition of metal oxyhydroxides, such as FeOOH and CoOOH, on the surface of Al-doped $SrTiO_3$ particles was aimed to improve some essential characteristics for the photocatalytic process, namely: increase of the specific adsorption surface area, extension of the light absorption range and efficient separation of photogenerated species.

- The $Al_{3\%}$:$SrTiO_3$@MOOH (M=Fe, Co) nanocomposites were obtained using modified precipitation processes, for FeOOH four materials corresponding to its four polymorphic forms were synthesized. The results of XRD analysis confirmed the crystallographic phases corresponding to the deposited oxyhydroxides, as well as the characteristic perovskite phase of $SrTiO_3$.
- The photocatalytic activity of the FeOOH-deposited materials was evaluated by performing photocatalytic degradation tests of Orange IV dye, the results indicating that the nanocomposite $Al_{3\%}$:$SrTiO_3$@δ-FeOOH is the most efficient of the studied ones.

- The process used to deposit the δ-FeOOH polymorph on the surface of $Al_{3\%}$:$SrTiO_3$ nanoparticles led to the obtention of a material characterized by high surface adsorption, ability to absorb visible radiation and remarkable photocatalytic activity. The enhanced photocatalytic efficiency obtained in photodegradation processes is considered to be the result of the synergistic effect obtained by the coupling of the two semiconductors.

- The results obtained from the active species determination tests correlated with the electronic structure information and LC-MS analysis results allowed to propose distinct mechanisms to explain the degradation process of the dye and the degradation mechanism of the antibiotic by identifying some of the degradation products.

- Photocatalytic tests performed using as photocatalyst the nanocomposite obtained by depositing CoOOH on the $Al_{3\%}$:$SrTiO_3$ surface indicated that it exhibits photocatalytic activity in the photodegradation of oxacillin.

- The results obtained for the two nanocomposites suggest that the deposition of oxyhydroxides on the $SrTiO_3$ surface led to materials that exhibit enhanced photocatalytic activity under the action of visible-field radiation and can be used as efficient photocatalysts in the degradation of various pollutants in wastewater as well as in the photocatalytic water splitting.

Selective bibliography

[5] J.A. Rodríguez, M. Fernández-García, Introduction the World of Oxide Nanomaterials, in: J.A. Rodríguez, M. Fernández-García (Eds.), Synth. Prop. Appl. Oxide Nanomater., 1st ed., Wiley, 2007: pp. 1–5. https://doi.org/10.1002/9780470108970.ch.

[6] D. Nunes, A. Pimentel, L. Santos, P. Barquinha, L. Pereira, E. Fortunato, R. Martins, Introduction, in: Met. Oxide Nanostructures, Elsevier, 2019: pp. 1–19. https://doi.org/10.1016/B978-0-12-811512-1.00001-1.

[7] K. Dey, Metal Oxide Nanomaterials: An Overview, in: A. Srivastava (Ed.), Oxide Nanostructures, Pan Stanford Publishing, 2014: pp. 1–98. https://doi.org/10.1201/b15633-2.

[8] K. Haas, Application of Metal Oxide Nanoparticles and their Economic Impact, in: O. Diwald, T. Berger (Eds.), Met. Oxide Nanoparticles, 1st ed., Wiley, 2021: pp. 29–65. https://doi.org/10.1002/9781119436782.ch2.

[9] T. Tatarchuk, M. Bououdina, J. Judith Vijaya, L. John Kennedy, Spinel Ferrite Nanoparticles: Synthesis, Crystal Structure, Properties, and Perspective Applications, in: O. Fesenko, L. Yatsenko (Eds.), Nanophysics Nanomater. Interface Stud. Appl., Springer International Publishing, Cham, 2017: pp. 305–325. https://doi.org/10.1007/978-3-319-56422-7_22.

[32] A. Žužić, A. Ressler, J. Macan, Perovskite oxides as active materials in novel alternatives to well-known technologies: A review, Ceram. Int. 48 (2022) 27240–27261. https://doi.org/10.1016/j.ceramint.2022.06.152.

[59] A. Pandikumar, K. Jothivenkatachalam, Photocatalytic functional materials for environmental remediation, John Wiley & Sons, Inc, Hoboken, NJ, 2019.

[63] M. Irshad, Q.T. Ain, M. Zaman, M.Z. Aslam, N. Kousar, M. Asim, M. Rafique, K. Siraj, A.N. Tabish, M. Usman, M.U. Hassan Farooq, M.A. Assiri, M. Imran, Photocatalysis and perovskite oxide-based materials: a remedy for a clean and sustainable future, RSC Adv. 12 (2022) 7009–7039. https://doi.org/10.1039/D1RA08185C.

[64] R. Ameta, M.S. Solanki, S. Benjamin, S.C. Ameta, Photocatalysis, in: Adv. Oxid. Process. Waste Water Treat., Elsevier, 2018: pp. 135–175. https://doi.org/10.1016/B978-0-12-810499-6.00006-1.

[69] Z. Wang, C. Li, K. Domen, Recent developments in heterogeneous photocatalysts for solar-driven overall water splitting, Chem. Soc. Rev. 48 (2019) 2109–2125. https://doi.org/10.1039/C8CS00542G.

[72] Q. Wang, K. Domen, Particulate Photocatalysts for Light-Driven Water Splitting: Mechanisms, Challenges, and Design Strategies, Chem. Rev. 120 (2020) 919–985. https://doi.org/10.1021/acs.chemrev.9b00201.

[74] T. Takata, K. Domen, Particulate Photocatalysts for Water Splitting: Recent Advances and Future Prospects, ACS Energy Lett. 4 (2019) 542–549. https://doi.org/10.1021/acsenergylett.8b02209.

[88] D. Gherca, A. Pui, N. Cornei, A. Cojocariu, V. Nica, O. Caltun, Synthesis, characterization and magnetic properties of MFe_2O_4 (M=Co, Mg, Mn, Ni)

nanoparticles using ricin oil as capping agent, J. Magn. Magn. Mater. 324 (2012) 3906–3911. https://doi.org/10.1016/j.jmmm.2012.06.027.
[104] A. Jakimińska, M. Pawlicki, W. Macyk, Photocatalytic transformation of Rhodamine B to Rhodamine-110 – The mechanism revisited, J. Photochem. Photobiol. Chem. 433 (2022) 114176. https://doi.org/10.1016/j.jphotochem.2022.114176.
[123] R. Di Capua, M. Radovic, G.M. De Luca, I. Maggio-Aprile, F. Miletto Granozio, N.C. Plumb, Z. Ristic, U. Scotti Di Uccio, R. Vaglio, M. Salluzzo, Observation of a two-dimensional electron gas at the surface of annealed $SrTiO_3$ single crystals by scanning tunneling spectroscopy, Phys. Rev. B - Condens. Matter Mater. Phys. 86 (2012) 1–6. https://doi.org/10.1103/PhysRevB.86.155425.
[124] A. Chikina, F. Lechermann, M.A. Husanu, M. Caputo, C. Cancellieri, X. Wang, T. Schmitt, M. Radovic, V.N. Strocov, Orbital ordering of the mobile and localized electrons at oxygen-deficient $LaAlO_3/SrTiO_3$ interfaces, ACS Nano 12 (2018) 7927–7935. https://doi.org/10.1021/acsnano.8b02335.
[125] V.N. Strocov, F. Lechermann, A. Chikina, F. Alarab, L.L. Lev, V.A. Rogalev, T. Schmitt, M.A. Husanu, Dimensionality of mobile electrons at x-ray-irradiated $LaAlO_3/SrTiO_3$ interfaces, Electron. Struct. 4 (2022). https://doi.org/10.1088/2516-1075/ac4e74.
[126] V.N. Strocov, A. Chikina, M. Caputo, M.A. Husanu, F. Bisti, D. Bracher, T. Schmitt, F. Miletto Granozio, C.A.F. Vaz, F. Lechermann, Electronic phase separation at $LaAlO_3/SrTiO_3$ interfaces tunable by oxygen deficiency, Phys. Rev. Mater. 3 (2019) 1–9. https://doi.org/10.1103/PhysRevMaterials.3.106001.
[127] Z. Zhao, R.V. Goncalves, S.K. Barman, E.J. Willard, E. Byle, R. Perry, Z. Wu, M.N. Huda, A.J. Moulé, F.E. Osterloh, Electronic structure basis for enhanced overall water splitting photocatalysis with aluminum doped $SrTiO_3$ in natural sunlight, Energy Environ. Sci. 12 (2019) 1385–1395. https://doi.org/10.1039/c9ee00310j.
[129] F.M.F. de Groot, J. Faber, J.J.M. Michiels, M.T. Czyiyk, M. Abbate, J.C. Fuggle, Oxygen 1s x-ray absorption of tetravalent titanium oxides: A comparison with single-particle calculations, Phys. Rev. B - Condens. Matter Mater. Phys. 48 (1993) 2074–2080.
[147] Q. Zhang, L. Jiang, J. Wang, Y. Zhu, Y. Pu, W. Dai, Photocatalytic degradation of tetracycline antibiotics using three-dimensional network structure perylene diimide supramolecular organic photocatalyst under visible-light irradiation, Appl. Catal. B Environ. 277 (2020) 119122. https://doi.org/10.1016/j.apcatb.2020.119122.
[148] X. Yu, J. Wang, X. Fu, H. Meng, Y. Zhu, Y. Zhang, Construction of Z-scheme $SrTiO_3/Ag/Ag_3PO_4$ photocatalyst with oxygen vacancies for highly efficient degradation activity towards tetracycline, Sep. Purif. Technol. 241 (2020) 116718. https://doi.org/10.1016/j.seppur.2020.116718.

[149] L. Wu, W. Wang, S. Zhang, D. Mo, X. Li, Fabrication and Characterization of Co-Doped Fe_2O_3 Spindles for the Enhanced Photo-Fenton Catalytic Degradation of Tetracycline, ACS Omega 6 (2021) 33717–33727. https://doi.org/10.1021/acsomega.1c04950.
[150] X. He, T. Kai, P. Ding, Heterojunction photocatalysts for degradation of the tetracycline antibiotic: a review, Environ. Chem. Lett. 19 (2021) 4563–4601. https://doi.org/10.1007/s10311-021-01295-8.
[151] S. Song, H. Bao, X. Lin, X.-L. Du, J. Zhou, L. Zhang, N. Chen, J. Hu, J.-Q. Wang, Molten salt-assisted synthesis of bulk CoOOH as a water oxidation catalyst, J. Energy Chem. 42 (2020) 5–10. https://doi.org/10.1016/j.jechem.2019.05.021.
[152] Justin Gorham, NIST X-ray Photoelectron Spectroscopy Database - SRD 20, (2012). https://doi.org/10.18434/T4T88K.
[157] X. Yang, Z. Chen, W. Zhao, C. Liu, X. Qian, M. Zhang, G. Wei, E. Khan, Y. Hau Ng, Y. Sik Ok, Recent advances in photodegradation of antibiotic residues in water, Chem. Eng. J. 405 (2021) 126806. https://doi.org/10.1016/j.cej.2020.126806.

Papers published in Web of Science impact factor journals

1. **Radu, I.**, Turcan, I., Lukacs, A. V., Roman, T., Bulai, G. A., Olariu, M. A., Dumitru, I., Pui, A., "Structural, dielectric and gas sensing properties of gadolinium (Gd^{3+}) substituted zinc-manganese nanoferrites", Polyhedron, 221, 115893, 2022 (**IF = 2,4**);

2. **Radu, I.**, Borhan, A. I., Ghercă, D., Popescu, D. G., Borca, C. N., Huthwelker, T., Bulai, G., Stoian, G., Husanu, M. A., Pui, A., "Enhancement of $SrTiO_3$ photocatalytic efficiency by Al doping: Answers from the structure, morphology and electronic properties contributions", Ceramics International, 50(11), 20664-20675, 2024 (**IF = 5,1**);

3. **Radu, I.**, Borhan, A. I., Ghercă, D., Dirtu, A. C., Dirtu, D., Popescu, D. G., Husanu, M. A., Pui, A., "Cobalt oxyhydroxide co-catalyst loaded onto Al:$SrTiO_3$ surface to boost photocatalytic performance", Materials Chemistry and Physics, 332, 130274, 2025 (**IF = 4,3**).

Total impact factor: 11,8